High-Fidelity Modeling of Turbulent Mixing and Basal Melting in Seawater Intrusion Under Grounded Ice

Madeline S. Mamer [1], Alexander A. Robel [1], Chris C. K. Lai [2], Earle Wilson [3], and Peter Washam [4]

[1]Georgia Institute of Technology, Department of Earth and Atmospheric Sciences
[2]Georgia Institute of Technology, Department of Civil and Environmental Engineering
[3]Stanford University, Department of Earth System Science
[4]Cornell University, Department of Astronomy

Correspondence: Madeline Mamer (mmamer3@gatech.edu)

Abstract.

Small-scale ice-ocean interactions near and within grounding zones play an important role in determining the current and future contribution of marine ice sheets to sea level rise. However, the processes mediating these interactions are represented inaccurately in large-scale coupled models and thus contribute to uncertainty in future projections. Due to limited observa-

5 tions and computational resources, grounding zone fluid dynamics in ice sheet models are simplified, omitting potential fluid exchange across the grounding zone. Previous modeling studies have demonstrated that seawater can interact with subglacial discharge upstream of the grounding zone and recent observations appear to support this possibility. In this study, we investigate turbulent mixing of intruded seawater and glacial meltwater under grounded ice using a high-fidelity computational fluid dynamics solver. In agreement with previous work, we demonstrate the strongest control on intrusion distance is the speed of

10 subglacial discharge and the geometry of the subglacial environment. We show that, in some cases, turbulent mixing can reduce intrusion distance, but not prevent intrusion entirely. Basal melting from seawater intrusion produces buoyant meltwater which acts as an important negative feedback by reducing near-ice thermohaline gradients. Modeled basal melt rates from seawater intrusion exceed melt rates predicted by existing sub-ice shelf melt parameterizations, which make assumptions about the structure of the near-ice boundary layer that do not hold where seawater intrudes into fresh subglacial discharge. We conclude

15 that, during periods of slow subglacial discharge, seawater intrusion can be an important mechanism of ocean-forced basal melting of marine ice sheets.

1 Introduction

Marine-terminating glaciers in Greenland and Antarctica have experienced accelerating ice loss over the past several decades (Otosaka et al., 2023). Ocean melting of marine-terminating glaciers has driven a considerable amount of this mass loss (De-

20 poorter et al., 2013; Rignot et al., 2013), but is not yet accurately represented within current coupled ice-ocean models. Efforts to improve coupled models focus on improving current parameterizations of melt rates at the ice-ocean interface (Kimura et al., 2015; Middleton et al., 2022; Zhao et al., 2024; Washam et al., 2023), collecting in-situ data (Stanton et al., 2013; Christianson et al., 2016; Jackson et al., 2017; Washam et al., 2020; Davis et al., 2023; Schmidt et al., 2023), and uncovering novel melt

mechanisms not included in current coupled models (Rosevear et al., 2021, 2022). In this study, we focus on fluid processes
25   that mediate one such novel melt mechanism under grounded ice.

Grounding lines are junctions between the grounded and floating portions of ice sheets. The grounding line has historically
been considered to be a hydraulic barrier between the cold, fresh subglacial hydrologic system and the relatively warm, saline
ocean. Models have suggested that tidal forcing may push seawater upstream of the grounding line (Sayag and Worster,
2013; Walker et al., 2013), causing tidally asymmetric melt in this "grounding zone" region (Gadi et al., 2023). Recent field
30   observations have suggested that this zone is hydraulically active, with mixing occurring between the ocean and subglacial
hydrology upstream of the grounding line (Macgregor et al., 2011; Horgan et al., 2013; Whiteford et al., 2022; Kim et al.,
2024). Satellite observations find evidence for elevated rates of basal melt at and beyond the grounding line relative to near-
zero values typically expected for grounded ice, contributing to retreat (Milillo et al., 2019; Ciracì et al., 2023).

More recently, seawater intrusion within and beyond grounding zones has been hypothesized to behave similarly to flow in
35   estuaries, developing a wedge-shaped density front at which fresh glacier melt discharge flows over inflowing saline seawater.
Wilson et al. (2020) and Robel et al. (2022) adapted a theoretical model for layered shallow water flows in estuaries (e.g.,
Krvavica et al., 2016) to demonstrate mathematically that freshwater velocity, the geometry of the subglacial environment,
and the wall drag acting on the fluid all potentially exert important controls on the extent of seawater intrusion in subglacial
hydrological systems. Due to the stratified nature of a salt wedge and lower fluxes, Robel et al. (2022) has hypothesized that ice
40   loss from seawater intrusion is driven by double-diffusive convection. More recent work has proposed that enlargement of the
cavity under grounded ice via shear-driven melting enhances seawater intrusion and may lead to a run-away positive feedback
if melting outpaces ice advection (Bradley and Hewitt, 2024).

Prior theories of ocean-driven melt have emphasized the importance of turbulent mixing in driving heat and salt transport
towards the ice-ocean interface (McPhee, 2008) and creating fully mixed boundary layers adjacent to the ice. Traditional melt
45   parameterizations rest on this assumption of an ice-adjacent fully mixed boundary layer (Jenkins, 2011), however, in regions
of seawater intrusion such assumptions may not hold. Within domains of seawater intrusions, a layer of buoyant freshwater
lies above a dense salt wedge in a stratified environment (Wilson et al., 2020), with a boundary layer that evolves along
the length of the seawater intrusion. This means the near-ice salinity goes to zero and the equation of state changes, and
is therefore a distinctly different regime than the assumptions inherent in current melt parameterizations. Turbulent mixing
50   can be a mechanism that reduces stratification by enhancing interfacial mixing between the salt wedge and freshwater layer,
transporting heat and salt upward into the ice-adjacent freshwater layer. Conversely, excess buoyant forcing from basal melting
induced by seawater intrusion may inhibit intrusion by increasing total freshwater discharge. Prior studies of seawater intrusion
have omitted turbulent mixing in the interest of obtaining simple mathematical theories and have not considered feedbacks
between intrusion-induced melting and intrusion persistence. In this study, we investigate these effects with the aid of a high-
55   fidelity computational fluid dynamics solver, with three aims: (1) to test previously proposed controls on seawater intrusion
distance, (2) to determine the effects of turbulent mixing on seawater intrusion, and (3) to investigate the dynamics of intrusion-
caused basal melting.

2 Methods

To study the dynamics of seawater intrusion beneath grounded ice, we utilized ANSYS Fluent (ANSYS, 2022), a high-fidelity

60 computational fluid dynamics (CFD) solver of the Reynolds-Averaged Navier Stokes (RANS) equations using the finite vol-
ume method. Using a high-fidelity CFD solver allows the simulations to have model resolutions on the scale of millimeters.
Unlike previous studies, by using this CFD solver at such fine resolution, we are able to resolve heat and mass transfer through
the entire water column, and appropriate turbulence closure schemes allow for the boundary layer to be resolved. We consider a
two-dimensional subglacial domain, encompassing one vertical and one horizontal (orthogonal to the local grounding line) di-

65 mension. The domain is akin to an unbounded freshwater sheet that meets the ocean at a specified discharge point, representing
the grounding line. Since we do not resolve ice dynamics, we delineate a grounding line instead of a grounding zone to reduce
the domain size and limit geometric constraints to an idealized subglacial water sheet. The geometry of the bounding surfaces
in this configuration is constant, with the vertical ice front chosen to limit the geometric influences on intrusion distance to only
within the subglacial environment. Tides are not considered in this study, which would temporally alter the geometry of the

70 subglacial environment and therefore be another factor influencing intrusion distance. The underlying bedrock has no perme-
ability, and the subglacial environment between ice and bedrock is unobstructed by obstacles, both of which would introduce
further controls on intrusion distance (Robel et al., 2022).

2.1 Domain and Boundary Conditions

Figure 1 depicts the standard model configuration we use in this study. There are two velocity inlets common to all simulations:

75 a seawater source at the inlet boundary of the tall ocean basin (dark blue arrow in Figure 1) and a freshwater source at the inlet
boundary of the subglacial environment (light blue arrow in Figure 1). In describing the results, we utilize the convention of
downstream being towards the ocean basin and the upstream being towards the freshwater inlet. The seawater inlet velocity is
prescribed as u_o across all cases, acting as a sustaining source of saline warm water to the model domain. Initial simulations
(Figure A2) indicate that the seawater inflow speed does not have a qualitative influence on the seawater intrusion over a range

80 of relatively weak ocean current speeds that we consider appropriate for the constrained ocean cavity near the grounding line
$(0.05 - 5$ cm/s), so we set $u_o = 0.5$ cm/s for all simulations going forward. The freshwater velocity, u_f, is varied over three
orders of magnitude $(0.05 - 5$ cm/s) to mimic a range of likely subglacial discharge velocities (Carter et al., 2017; Davis et al.,
2023; Washam et al., 2020) in Antarctica and Greenland in non-summer months and previous experimentally tested speeds
(Wilson et al., 2020). Similarly, a pressure outlet boundary (red arrow in Figure 1) is prescribed in the ocean basin employing

85 a zero gradient flux at the boundary and ensuring mass conservation in the model. Finally, vertical and horizontal ice wall
boundaries (where the ice is in contact with the fluid domain) are defined with characteristics that mimic a grounding line
environment. The ice wall boundaries have a temperature boundary condition of $0°C$ and a no-slip kinematic condition which
forces the freestream fluid velocity to be zero at the ice wall. The vertical ice front in this configuration resembles a tidewater
glacier and is utilized to restrict the geometric controls on intrusion distance to those within the subglacial environment.

90 Having a low-sloping ice-shelf bottom would introduce further constraints on the ability for seawater to intrude beyond the

grounding line since intrusion distance is a function of the height of its environment (Robel et al., 2022; Wilson et al., 2020). Such a configuration would also require computational domains much larger than are feasible to simulate at the resolution needed to properly resolve the ice-water boundary layer. Despite the tidewater-like geometric configuration, the low subglacial discharge fluxes make the fluid domain appropriate for simulating conditions expected in Antarctica year-round or Greenland

95   in non-summer months. The "subglacial environment" is the domain upstream of the grounding line. Since the bedrock and ice-adjacent boundary layer thicknesses depend on the freestream fluid velocities, the mesh resolution changes for each freshwater velocity to accurately model near-wall processes with the chosen turbulence closure scheme. Our vertical domain size is at the upper bound of the viscous sublayer length scale that could exist between a well-mixed boundary layer and the ice (i.e. the vertical domain is small and does not include the turbulent outer layer). Further discussion on domain and meshing is included

100   in sections A1 and A2.

2.2 Salt and Heat Transport

In addition to solving the RANS equation for fluid velocities, we configure the CFD solver to calculate the concentration of salt with a "species transport model" (advection-diffusion equations) (ANSYS, 2009). The seawater inlet is prescribed with 30 ppt salinity and $T_o = 0.5°C$ while the freshwater inlet is prescribed with zero salinity and $T_f = 0°C$. Seawater temperature

105   is chosen to represent warm cavity Antarctic conditions (Middleton et al., 2022; Kimura et al., 2015). Seawater salinity is set to generate a water mass with density characteristic of the Southern Ocean. The species transport model also calculates water density (ρ_w) with a prescribed equation of state from Roquet et al. (2015)

$$\rho_w = 1000 + S_w * (0.7718 * 1000) + (T_w - 273.15) * (-0.1775) \tag{1}$$

The salinity, S_w, and temperature, T_w, of the fluid are found at the center of each cell. This simplified linear equation of state

110   was chosen for ease of implementation as a user-defined function within ANSYS Fluent and with the assumption that cabelling or thermobaricity do not play a role in this environment. Energy, and therefore fluid temperature, is evolved via an energy conservation equation employed by the CFD solver resolving advection, conduction, diffusion, and molecular dissipation (ANSYS, 2009). Since heat and salt transport are solved independently of this linear equation of state, double-diffusive mixing can still be simulated. Further details of heat and salt transport in the model can be found in section A4.

115 ## 2.3 Turbulence Closure Scheme

Turbulent mixing can increase the exchange of heat and salt between seawater and fresh subglacial discharge, homogenizing the water column and potentially reducing the ability for seawater to intrude. The theory of Wilson et al. (2020) assumes no mixing between the two water masses, treating the interfacial drag (which dictates shear) as a free parameter dependent on fluid flow. Robel et al. (2022) treats interfacial drag as negligible to derive a closed-form prediction for intrusion distance.

120   However, under scenarios of fast subglacial discharge, the experiments described in Wilson et al. (2020) exhibited interfacial mixing with the formation of wave crests at the top of the salt wedge. To understand the role turbulent mixing has in a seawater intrusion regime, we enable the commonly used $\kappa - \epsilon$ two-equation turbulence closure scheme (Mansour et al., 1989; Launder
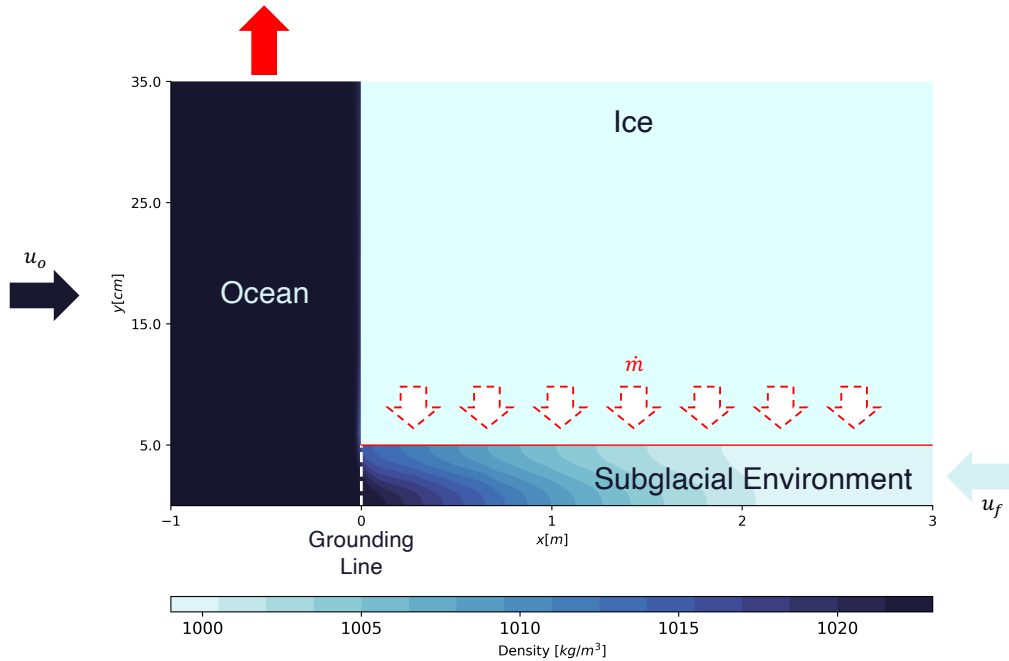
Figure 1. Schematic of the domain used in ANSYS Fluent. Ice block is not simulated and used to graphically depict the vertical and horizontal (red solid line) ice-ocean interfaces. The length of the subglacial environment is 30 m and height 5 cm. The ocean basin is 2 m wide by 5 m tall. The dark blue arrow on the left represents seawater input (u_o), while the light blue arrow on the right represents freshwater input (u_f). The solid red arrows represent outflows. The outlined red arrows represent the meltwater input ($\dot{m}$) that is turned on for the 'melt-enabled' cases as a function of near-wall temperature (eq. 4).

and Spalding, 1983). A closure scheme is necessary because averaging the RANS equations introduces Reynolds stresses due to turbulent motion within the fluid. These take the form $\overline{(u'v')}$, the averaged product of turbulent velocity fluctuations in the x

125 and y direction. The $\kappa - \epsilon$ two-equation model solves for these stresses by assuming that the Reynolds stresses are a function of eddy viscosity, μ_t, following the Boussinesq hypothesis (Schlichting and Gersten, 2016). The eddy viscosity is then solved for by

$$\mu_t = \rho_w C_\mu \frac{\kappa^2}{\epsilon},$$ (2)

where κ represents the turbulent kinetic energy, ϵ represents dissipation, and ρ_w is the water density. This form of turbulence closure provides an avenue to manipulate the degree of turbulent mixing by modulating the parameter C_μ. This is a model parameter that dictates the amount of turbulent transport (mixing) given some κ^2/ϵ. Larger values of C_μ imply that the flow is more turbulent because the eddy viscosity and consequently Reynolds stresses are increased. We vary this parameter across a factor of four (0.045, 0.09, 0.18) which allows us to explore a range of possible turbulent mixing while maintaining model stability. The middle value is commonly adopted as the "standard value" and is derived from experiments with equilibrium shear flows e.g., the log-law region and above in pipe flows. We employ the low-Reynolds formulation of the $\kappa - \epsilon$ closure scheme which uses damping equations near wall boundaries to adequately resolve the viscous sublayer, allowing for finer resolution near the ice boundaries and complete boundary layer resolution (Hrenya et al., 1995; ANSYS, 2009). Within the model framework here, the wall drag coefficient is not a free parameter to be set, but rather diagnosed from the simulations via the relationship

$$C_d = u_*^2/u^2 \tag{3}$$

where u_* is the shear velocity and u is the free stream current speed (McPhee, 1979).

2.4 Basal Melting

In some simulations, we also simulate the added buoyancy flux resulting from melting at the horizontal ice wall by changing it from a wall boundary condition to a velocity inlet (red dashed arrows in Figure 1). In ANSYS Fluent, a wall boundary condition holds a constant temperature while providing a shearing force on the fluid in accordance with the no-slip wall boundary condition. When changed to a velocity inlet, the inflowing melt can have a prescribed temperature and salinity but does not provide any source of shear. Melting is only turned on for the horizontal ice face (red line in Figure 1) and not the vertical ice face to isolate the added buoyancy effects from seawater intrusion forced melt only. The vertical ice face is susceptible to plume-driven melt from the buoyant subglacial discharge (Figure A7) and is distinctly different than the seawater intrusion melt domain. The horizontal ice velocity inlet speed is set by the melt rate, $\dot{m}$, and is a function of the difference between the near-wall cell's centroid temperature T_w and ice-ocean interfacial temperature T_i, thermal conductivity κ_T, and density of the ice ρ_i:

$$\dot{m} = \frac{\kappa_T}{\rho_i L_i} \frac{T_w - T_i}{0.5 H_c}. \tag{4}$$

The thermal forcing is divided by half of the near-wall cell height, H_c, to obtain the near-wall thermal gradient, $\partial T/\partial z$. L_i is the latent heat of ice. The values of all constants are presented in Table A1. This framework represents the conservation of heat at the ice-ocean interface which we can use to calculate melt rates instead of a parameterization because we resolve the boundary layer directly and so do not need to make assumptions about how heat and salt are transported through the boundary layer. Inherent in this is the assumption ANSYS Fluent accurately simulates all appropriate boundary layer transport processes necessary to get heat from the freestream fluid flow to the cell grid next to the ice face, and any melting experienced is due

160   to the conservation of heat at the ice-adjacent cell. An alternative to this formulation would be to replace κ_T with the product of thermal diffusivity (K_T), seawater density (ρ_w), and seawater heat capacity (c_w), allowing for varying seawater density to affect heat transfer to the boundary. However, back-of-envelope calculations show small variances in density ($\sim 20 \, \text{kg/m}^3$) lead to small changes ($< 5\%$) in the melt rate. Therefore, using a constant thermal conductivity is appropriate. Note the boundary does not move over time (as in Bradley and Hewitt, 2024) and an evolving geometry of the subglacial space is not tested in this

165   work. This choice greatly simplifies the computational domain and considerations of meshing with turbulent closures.

Each simulation is initialized by calculating the steady-state directly using the solver included in ANSYS Fluent. Using this steady-state solution as an initial state, the transient solver is then run for 12 hours at 5 second time steps. All results presented are from the transient simulations and a comparison to the steady-state solutions is shown in section A4 (Figure A1). A list of all simulations is presented in section A4 (Table A2).

170   3   Results

3.1   Characteristics of the Seawater Intrusion

In all simulations, warm seawater intrudes some distance beyond the defined grounding line ($x = 0$ m in Figure 2). A strong control on seawater intrusion distance is the freshwater discharge velocity, in line with previous work (Wilson et al., 2020; Robel et al., 2022; Krvavica et al., 2016). The simulation with the lowest flux of freshwater (Figure 2 C) has a 3.5 m intrusion,

175   while the fastest flux experiences only 15 cm of intrusion (Figure 2 B). This range of intrusion distances demonstrates a weaker dependence on freshwater velocity than suggested by Robel et al. (2022) where intrusion distance has an inverse quadratic dependence on freshwater velocity and therefore should vary by a factor of 1000. Turbulent mixing, as modulated by C_μ, affects intrusion distance to a lesser degree than freshwater discharge velocity when varied over a wide range encompassing likely values for realistic estuarine-like mixing rates. For the low and high freshwater velocity cases increased turbulent mixing

180   (dashed lines in Figure 2 B, C) increases intrusion distance. For the middle freshwater velocity (Figure 2 C), the time-averaged shift in the intrusion distance due to turbulent mixing is within the range of internal variability within a simulation due to turbulent mixing itself. To contrast the effects of turbulent mixing, we tested a laminar flow case with no turbulent mixing (green line Figure 2 A) and saw no meaningful difference in intrusion distance. This is not to say that turbulent mixing is unimportant in the dynamics of seawater intrusion, but rather that intrusion distance is not strongly sensitive to the strength

185   of turbulent mixing (over the range of discharge velocities and C_μ values considered realistic for subglacial and estuarine environments), particularly when compared to other factors such as the geometry of the subglacial environment and freshwater discharge flux. It may be that for much higher discharge velocities ($\mathcal{O}$(m/s)) encountered at times of high subglacial discharge, turbulent mixing plays a more important role than the cases considered here.

Changing subglacial geometry has a large effect on intrusion distance as demonstrated by the experiment with a taller

190   subglacial channel ($H = 7.5$ cm) plotted as a magenta line in Figure 2 A. Increasing the channel height by 50% increased the intrusion distance by nearly a factor of 3. This indicates an even stronger sensitivity to the height of the subglacial opening in these more realistic simulations than predicted by Robel et al. (2022), which finds a quadratic dependence on the subglacial
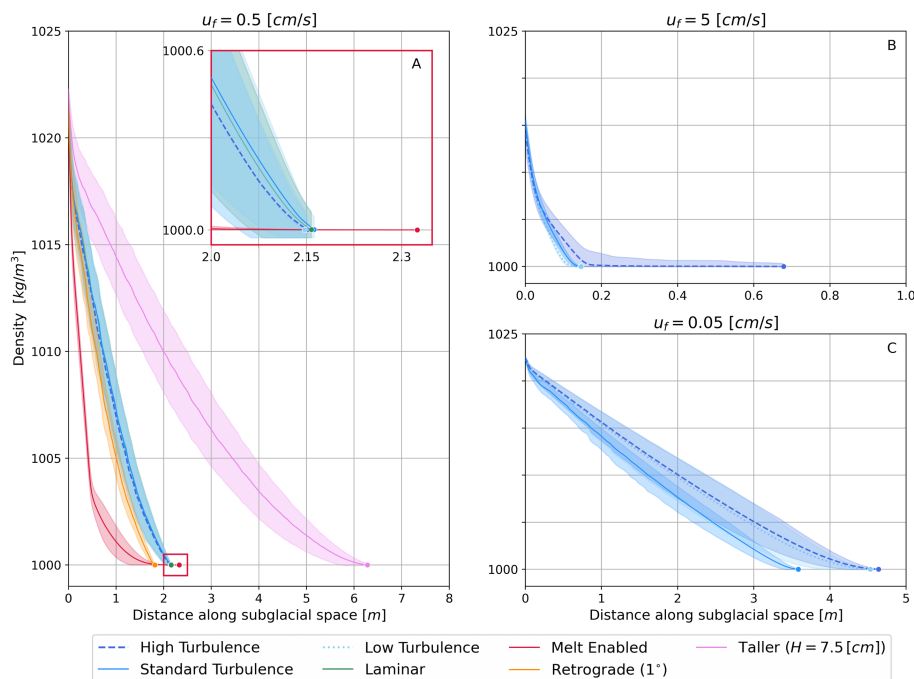
Figure 2. Density transects along the middle of the subglacial environment. The transect termini represents the intrusion distance or the point at which density is less than or equal to 1000 kg/m³. Blue lines represent non-melt-enabled scenarios, where the ice is held as a wall boundary and fixed temperature. Dashed lines represent higher turbulent mixing ($C_\mu = 0.18$), dotted lines are low turbulent mixing ($C_\mu = 0.045$), and solid lines are medium turbulent mixing ($C_\mu = 0.09$). The red transects are melt-enabled cases with medium turbulent mixing. Magenta and orange lines in panel A are scenarios with different geometries, a taller subglacial environment ($H = 7.5$ cm), and a retrograde slope ($\theta = 0.5°$) respectively. The green line in panel A is the laminar flow case with no turbulent mixing. Shading depicts the first temporal standard deviation or the maximum/minimum value depending on the smallest absolute difference with the average value. Pure seawater exists when $\rho_w = 1023$ kg/m³ and pure freshwater exists when $\rho_w = 1000$ kg/m³. Note the varying x-axis across the panels.

conduit height. We also tested the effects of a retrograde slope ($\theta = 0.5°$) on intrusion distance. In theory, a slanted base makes it easier for seawater to intrude due to the effect of gravity pushing dense seawater down slope, however, we saw no

195   noticeable difference between the flat and slanted cases (orange line Figure 2 A). Increasing the slope to $1°$ did nominally increase intrusion distance relative to the flat geometric cases (green line Figure A3). However, we did not find any evidence for an unbounded increase in the intrusion distance under these retrograde slopes as was predicted by (Wilson et al., 2020) and (Robel et al., 2022). That being said, our finite domain length may limit the intrusion distances achievable in this model configuration.

200   Vertical profiles of temperature, salinity, and velocity along the intrusion for non-melt-enabled cases (Figure 3) depict a two-layered flow in opposing directions, with a relatively uniform low-sloping vertical gradient in salinity, and a strong thermocline in the 2 cm directly below the ice. Such a steep thermocline is most likely due to the temperature boundary condition we
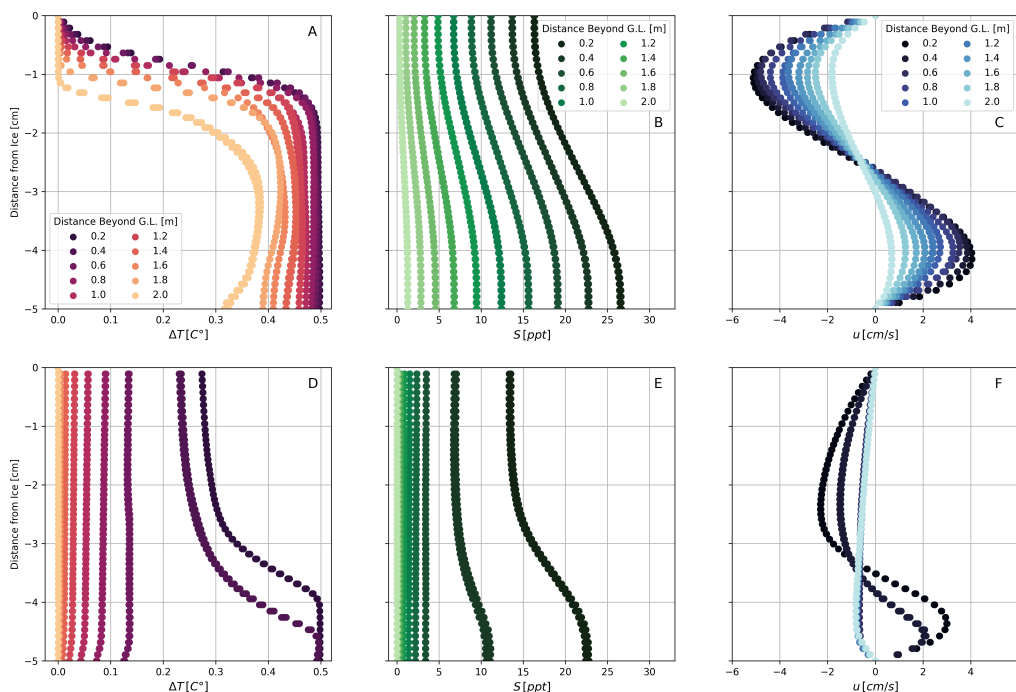
Figure 3. Vertical profiles of temperature (A, D), salinity (B, E), and x-component of velocity (C, F) along the seawater intrusion for $u_f = 0.5$ cm/s and medium turbulence $C_\mu = 0.09$. The distance beyond the grounding line represents the distance (m) upstream of the fixed grounding line. The top row (A, B, C) is for the non-melt enabled case, i.e. the horizontal ice boundary is a wall boundary with a fixed temperature. The bottom row (D, E, F) is for the melt-enabled case where the ice boundary becomes a velocity inlet with freshwater inflow as a function of near-wall temperature.

imposed on the horizontal ice boundary. This temperature boundary condition does not appear in the melt-enabled cases (panels D-F in Figure 3) where the thermocline is displaced downwards in the water column by the added freshwater and consequently

205 uniform temperature conditions exist for the upper half of the subglacial space. Further discussion on the melt-enabled vertical profiles is in section 3.2. The vertical structure of the subglacial water column indicates a highly stratified and complex flow regime near the grounding line, which decays to a uniform classic pipe flow setting further upstream.

Drag from the ice shears fluid flow in the subglacial environment to have zero velocity at the ice, per the no-slip kinematic boundary condition. This shearing determines boundary layer thickness and therefore influences heat and salt transport towards

210 the ice. As discussed in section 2.3, within this modeling framework the drag coefficient cannot be prescribed, but rather diagnosed from the simulations (eq. 3). In previous work (Wilson et al., 2020; Robel et al., 2022), C_d is set to values around

10^{-3} derived from observed drag coefficients under sea ice, however here we diagnose C_d's in the range of 10^{-2} to 10^0 (Figure A5) over the region experiencing seawater intrusion. Such high drag is mostly due to the acceleration in both the upper freshwater layer and lower seawater layer in the region of intrusion. Both layers are confined to a smaller area than their respective sources and thus accelerate. The sharp reversal in flow along the salt-wedge interface acts like another boundary where the fluid shears to zero before reversing direction. The high C_d likely explains the much smaller intrusion distances simulated here compared to prior studies (Wilson et al., 2020; Robel et al., 2022), and is discussed in more detail in Section 4. Where intrusion occurs, the near-wall velocity gradient grows (darker lines in Figure 3 C, F and A8 E, F, I, L), increasing the shear velocity and drag. This velocity gradient is an important driver of heat flux to the ice, as discussed in later sections.

3.2 Dynamics of intrusion-induced melt

Intrusion distance does not vary significantly for most cases when basal melt of ice is included (red lines in Figures 2 A and A4), though it does change the vertical structure of intrusions. For all geometric configurations with $u_f = 0.5$ cm/s the modeled melt peaks at ~ 10 m/yr (Figure 5) with about a quarter of the intrusion distance experiencing melt rates close to this peak value. In simulations with the retrograde slope and thicker subglacial environment, the region of ice experiencing significant melt is greater than the standard flat case. The distribution of melt resembles the intrusion wedge, with maximum melting near the grounding line, tapering off to low values of mm/year. This secondary source of freshwater discharge due to melting at the horizontal ice-water interface ultimately leads to substantial changes in the flow regime within the subglacial environment by (1) decreasing the near-ice temperature and salinity gradients and (2) increasing the stratification of the water column.

Changing the boundary condition of the horizontal ice from a no-slip wall with a fixed temperature to a velocity inlet dynamically changes the structure of seawater intrusions. Melt-enabled cases have smaller thermohaline gradients near the ice relative to the non-melt-enabled cases (Figure 3). In the non-melt-enabled cases, the boundary condition forces the temperature to be $0°C$ at the ice wall, as demonstrated by Figure 3 A. Alternatively, the melt-enabled cases have no fixed temperature at the boundary, allowing the fluid to have uniform temperature profiles near the ice. This demonstrates that the boundary condition is important to setting the near-ice thermal gradients. The salinity forcing is handled differently, with no boundary condition in either melt-enabled or non-melting scenarios, and as such has gentler gradients near the ice. The salinity gradient is reduced for melt-enabled cases, with more uniform conditions near the ice similar to the temperature gradient. The added source of buoyancy from the meltwater displaces the intrusion downwards in the water column and causes a flattening of the seawater intrusion interface as seen in the red line in Figure 2 A. The strengthening of stratification within the subglacial environment from the buoyant melt discourages vertical mixing and decreases the interfacial slope of the seawater intrusion. Near-ice velocity gradients are reduced when melting is turned on, dynamically changing the evolution of the ice-parallel velocity component. Reduction in velocity gradients arises from an increase in stratification, suppressing turbulence, and the kinematic boundary condition being a velocity inlet and not a no-slip wall.

Buoyancy frequency, N^2 is a measure of the degree of stratification in the water column:

$$N^2 = \frac{-g}{\rho_0} \frac{d\rho}{dy}. \tag{5}$$
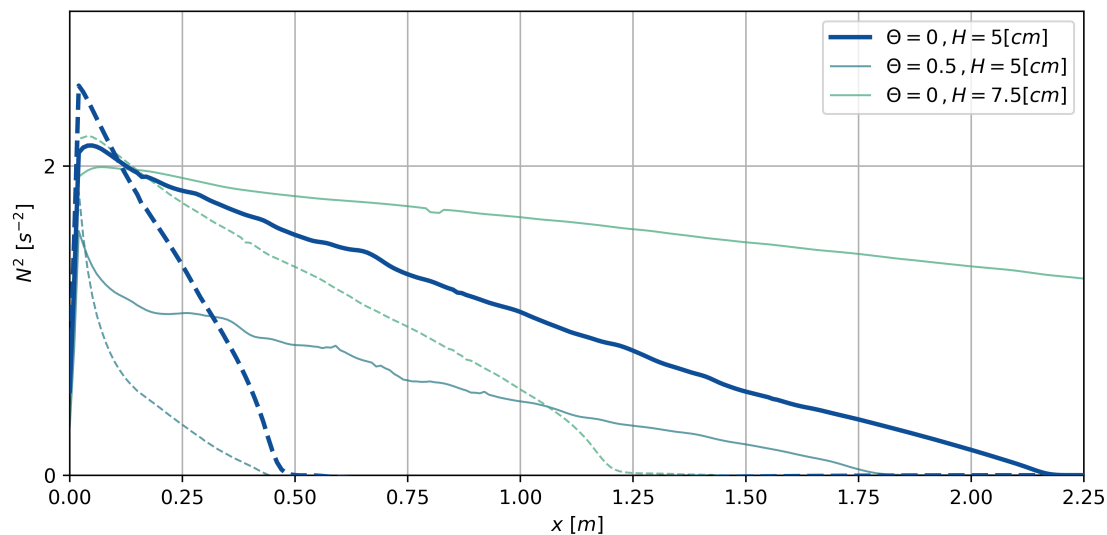
Figure 4. Buoyancy frequency (N^2) for $u_f = 0.5$ cm/s with the flat, retrograde, and thicker domain configurations. The solid lines are for non-melt-enabled cases and the dashed lines are for melt-enabled scenarios.

245   Figure 4 plots the buoyancy frequency along the subglacial environment with the vertical density gradient evaluated over the entire height of the subglacial environment. Higher N^2 indicates stronger density gradients and stratification, tracking the presence of seawater intrusion. When melt is enabled the horizontal extent of stratification in the subglacial environment is reduced, but where stratification occurs, it is stronger (Figure 4). In other words, the length of the seawater intrusion is reduced, but the stratification across its interface increases. Buoyant forcing, as represented by N^2, suppresses mixing in the

250   presence of a flat horizontal ice boundary (as we have here), competing with the velocity shear and turbulence that drive mixing over the length of the intrusion. In this sense, buoyant forcing can act to "shield" the ice from further melt, generating a near-ice layer of fresh, cold water. However, the horizontal density gradient introduced by the seawater intrusion will drive vertical convective motion, flattening isopycnals, and leading to additional interfacial shear and mixing. This convective-driven mixing mechanism differs from convective mixing caused by a sloping ice boundary, in which a buoyant plume may form.

255   For the idealized scenarios in this study, buoyant convection via ice geometry will not drive mixing and thus melt since the ice is perfectly horizontal. However, the vertical motion arising from the seawater intrusion's horizontal density gradient may be an important source of interfacial mixing, working in tandem with turbulence and double-diffusive convection to reduce stratification within the subglacial environment. Where subglacial openings have complex geometry, we anticipate buoyant-driven convection from sloping ice boundaries to aid in driving mixing on small scales which will reduce the stratification from

260   the intrusion and consequential melting.

    For every melt-enabled scenario, there is more than a 50% reduction in shear velocity near the wall relative to their non-melting cases. Shear at the ice-water interface, and consequentially the drag coefficient (Figure A5), is partially reduced from an

increase in stratification, suppressing turbulence. Further reduction in shear is most likely attributed to the boundary condition differences between melt-enabled and non-melting cases. At the ice face for melt-enabled cases, the flux boundary condition

265 replaces the kinematic no-slip boundary condition from the non-melt-enabled simulations. This means that for model runs where melting is turned on, the ice-parallel velocity component is not set to zero at the wall, unlike the non-melt-enabled cases. If a no-slip boundary condition could be imposed on the melt-enabled scenarios, the freestream velocity would likely be reduced due to the excess drag. This reduction in fluid velocity would then lessen the amount of mixing between the lower salt wedge and upper freshwater layer due to decreased interfacial shear decreasing the amount of heat being transferred to the ice

270 boundary and therefore decreasing melt.

3.3 Parameterization of basal melting in regions of seawater intrusion

Large-scale ocean and ice sheet models typically have grid resolutions much coarser than what is necessary to resolve the ice-ocean boundary layer and directly calculate heat and salt fluxes from the ocean towards the ice. In practice, parameterizations are used in large-scale models to approximate the melt rate based on ocean temperatures and salinities modeled outside the

275 boundary layer (10^1-10^4 meters) from the ice. However, such parameterizations have not previously been tested in the flow regimes relevant to seawater intrusion below grounded ice. Here, we simulate intrusion-induced basal melt by employing the conservation of energy (eq. 4) at the horizontal ice boundary and compare these model results directly to traditionally used parameterization schemes. In our simulations, we can accurately capture relevant boundary layer heat and salt transport processes and calculate basal melt rates because our model resolution of millimeters directly resolves the near-ice boundary

280 layer.

We consider three mechanisms that could drive mixing within the subglacial environment and heat and salt fluxes into the ice boundary. The first mechanism is shear, where the boundary layer thickness is set by the velocity of the freestream flow and the profile of velocity shear near the ice. A shear-driven regime typically leads to a well-mixed boundary layer, with relatively high freestream velocities and thus turbulence. This mechanism relies on the kinematics of the flow structure, rather than the

285 molecular or thermohaline properties of the fluid, to drive mixing. The second and third mechanisms are both convective, with the former being driven by buoyancy (natural convection) and the latter by diffusion (diffusive convection (DC)). Along sloped or vertical ice faces, natural convection occurs when fresh, light meltwater rises within denser ambient water, which can cause the mixing of seawater with ice-adjacent waters (McConnochie and Kerr, 2017; Cowton et al., 2015; Jenkins, 2011). For the flat domain configurations considered in this study, there are no ice boundary slopes in the direction of gravity (vertical), however,

290 horizontal density gradients arise due to seawater intrusion leading to baroclinic adjustment and vertical motion. Although what sets the convective instability differs, both processes rely on a sloped gravitational potential. The diffusion-dominated mixing mechanism relies on the molecular properties of heat and salt. Since heat and salt diffuse at different rates, a type of mixing known as double-diffusive convection (DDC) occurs. Here, since we do not simulate ice loss caused by salinity diffusion, we focus only on thermal diffusion (DC). We discuss the applicability and role of DDC in Antarctic-like settings in section 4.

295 The most widely used parameterization for modeling ocean-induced ice melt under ice shelves is the three-equation parameterization of Holland and Jenkins (1999) (referred to as S99), which assumes heat and salt transport occur via shear-driven

mixing. Here, we focus on the heat-limited melting ($\dot{m}_S$) case since our modeled melt only includes thermal forcing and our freezing point temperature is decoupled from salinity and pressure. Therefore we reduce the three equation parameterization to only the equation describing melt caused by the transfer of heat through the turbulent boundary layer:

$$\dot{m}_S L_i \rho_i = \rho_w c_w \gamma_T (T_w - T_i) - \rho_i c_i \kappa_i \frac{dT_i}{dy} \tag{6}$$

Here, L_i is the latent heat of ice, ρ_w is the seawater density, and c_w is the heat capacity of seawater. The product of the vertical temperature gradient of ice dT_i/dy, ice density ρ_i, the heat capacity of ice c_i, and the thermal conductivity of ice κ_i represents heat conduction into the ice. All values are presented in Table A1. We set the ice vertical temperature gradient to zero since we do not model any heat conduction within the ice and instead assume all energy is used to cause melting. The temperature of seawater and the ice-ocean interface are represented by T_w and T_i respectively. The turbulent transfer velocity, γ_T, describes the transfer of heat across the outer portion of the boundary layer and into the viscous sublayer adjacent to the ice. This transfer velocity is further parameterized via

$$\gamma_T = \frac{u_*}{2.12 \ln(u_* h \nu^{-1}) + 12.5 Pr^{2/3} - 9}, \tag{7}$$

where h is the distance of the chosen reference for T_w, usually taken to be the thickness of the viscous sublayer (Holland and Jenkins, 1999). The Prandtl number (Pr) is the ratio of viscous forces to diffusive forces for temperature (Kader and Yaglom, 1972; McPhee et al., 1987). The kinematic viscosity is represented by ν and the shear velocity, u_*, is defined as (Schlichting and Gersten, 2016)

$$u_* = \sqrt{\nu \frac{\partial u}{\partial y}} \tag{8}$$

however, it is generally solved as a quadratic function of the wall drag coefficient using equation 3. This means shear-driven parameterized melt rates are sensitive to the choice of drag coefficient (C_d). In this study, C_d is found to be 10^{-2} to 10^0, which is larger than the observed range for sea ice of 10^{-3} to 10^{-2} (Mcphee, 1980; Randelhoff et al., 2014; Brenner et al., 2021). In using shear velocity to drive the parameterization, this framework assumes the system has enough momentum to dictate boundary layer transport processes. When momentum is low, other processes like DC or natural convection may contribute to setting the complex boundary layer structure. For the weak flow scenarios tested here, we anticipate shear-driven turbulence to be relatively unimportant (Rosevear et al., 2022).

Diffusive-driven melt can occur in settings where stratification is strong and the shear-driven turbulence is weak or entirely absent. In these settings, the transfer of heat and salt is dictated by the thermal and haline molecular diffusivities (K_T, K_S), respectively. Molecular diffusion also occurs in any boundary setting within the viscous sublayer of the boundary layer, a thin layer adjacent to the ice. Heat fluxes caused by diffusive-driven transport take the form (Rosevear et al., 2021)

$$\dot{m}_{DC} = -\rho_w c_w K_T \frac{\partial T}{\partial y} \frac{1}{\rho_i L_i}, \tag{9}$$
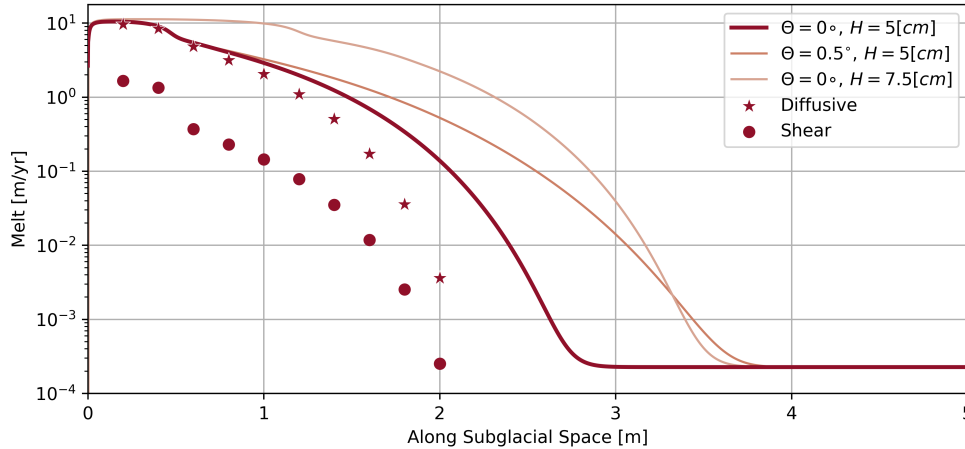
Figure 5. Comparison of modeled output and parameterized melt rates. The red lines represent the output of modeled melt from Fluent using equation 4 for $u_f = 0.5$ cm/s. Red scattered dots are the maximum S99 parameterized melt rates (Figure 6 a) at that location for $u_f = 0.5$ cm/s. Red stars are maximum diffusive parameterized melt rates (Figure 6 b) at that location for $u_f = 0.5$ cm/s.

where $\dot{m}_{DC}$ represents the melt rate. In Figure 5, we plot the basal melt rates calculated directly from our simulations assuming heat transfer across the mesh elements directly adjacent to the ice (lines) alongside melt rates calculated from the S99 parameterization (circles) and DC melt framework (stars) using a variety of assumptions related to their formulation discussed further below. The DC framework and S99 parameterization both underestimate melt throughout the entire intrusion domain, with the largest disagreement existing upstream closer to the transition from seawater to freshwater. In general, the S99 parameterization predicts melt rates in the range of $0.0001 - 1$ m/yr and the DDC framework predicts melt rates in the range $0.001 - 10$ m/yr. Thus, the melt rates calculated directly from these high-resolution simulations are generally more than an order of magnitude higher than those calculated using the S99 parameterization under any feasible assumptions about the mechanism driving melt and the structure of the boundary layer. There exists closer agreement between the DC framework and model output throughout the entire intrusion regime, particularly near the grounding line. However, that is expected due to the relationship between the thermal diffusivity, K_t, and the thermal conductivity, κ_T, used in our model framework. We consider the assumptions inherent in the formulation of these parameterizations in further detail below.

When using the S99 parameterization in large-scale models, T_w and S_w are generally taken some distance from the ice equal to or greater than the thickness of the boundary layer. Due to geometric constraints and the presence of two opposing flows, the boundary layer does not fully develop in our simulations, meaning the entire domain is within the boundary layer. Here, we tested the sensitivity of equations 6-9 to various choices of ice distance to obtain T_w, S_w, ρ_w, and u_*. All of the ice-ocean interfacial values (T_i, S_i) were found at the ice boundary and we set $\rho_i = 918$ kg/m^3. We take vertical profiles along the seawater intrusion for the $u_f = 0.5$ cm/s melt-enabled scenario (Figure 3) and compare the modeled melt to S99 parameterized melt. We evaluate the thermal turbulent transfer velocity γ_T (eq. 7) solving u_* (eq. 8) and h (distance from ice) at each point
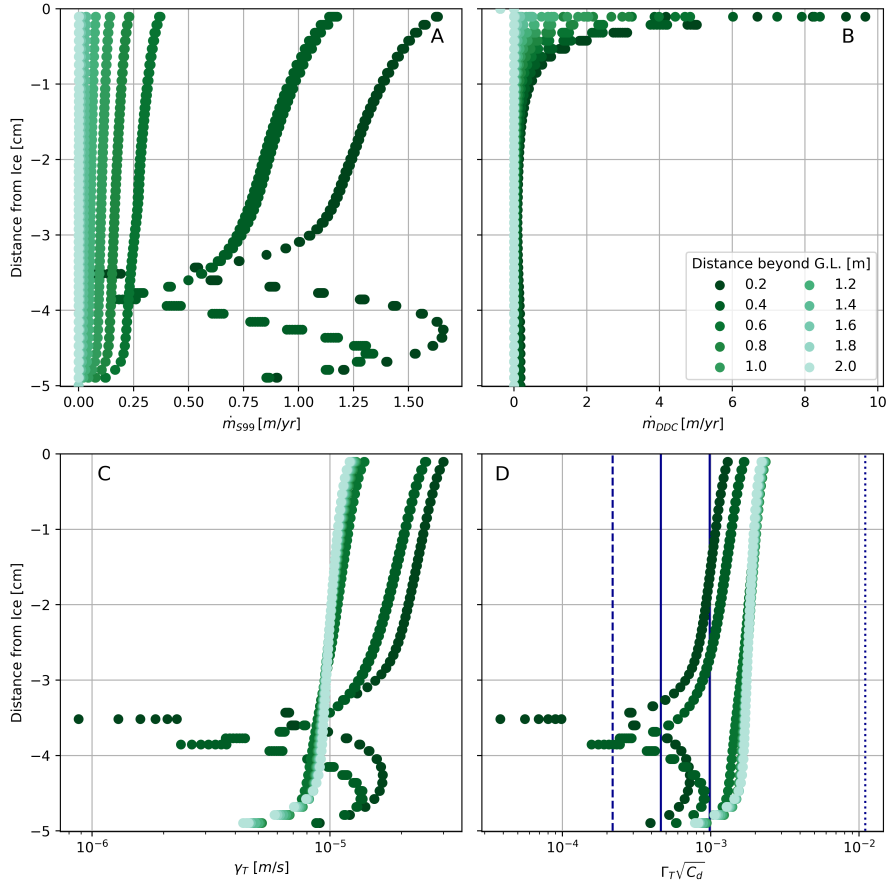
Figure 6. Sensitivity of basal melt rates to reference flow values obtained at different distances relative to the ice surface for a freshwater discharge rate of $u_f = 0.5$ cm/s with melting enabled. Panel A is the melt rate estimated using the shear-based parameterization (eq. 6) Panel B is the estimated melt rate in for the diffusive framework (eq. 9). Panel C is the thermal turbulent transfer (γ_T) coefficient evaluated with equation 7. Panel D is the thermal Stanton number which is equivalent to γ_T/C_d. The colors indicate vertical profiles taken at different distances from the grounding line, with darker colors representing closer to the grounding line. The blue lines represent previously published thermal Stanton numbers. The dotted is Jenkins et al. (2010), the dashed is Washam et al. (2020), and the solid from Washam et al. (2023).

345   within the vertical profile. The same steps are taken to evaluate the haline turbulent transfer velocity, γ_S, which is discussed in the section A6 since we are considering only the heat-driven melting scenario. We also use the corresponding point's T_w and S_w in equation 6. Results for γ_T and $\dot{m}_S$ are plotted in Figure 6 A, C, D.

In general, values for γ_T and their corresponding thermal Stanton numbers ($\sqrt{C_d}\Gamma_T$) calculated from our simulations are within the range found in the literature (Holland and Jenkins, 1999; Jenkins et al., 2010; Washam et al., 2023). Thermal
350   Stanton numbers represent the ratio of heat transfer to the thermal capacity of a fluid and indicate the balance of these two processes (Jenkins et al., 2010), whereas transfer velocities represent the efficacy of heat transport via turbulent and molecular

processes throughout the boundary layer. Stanton numbers are often used as tuning coefficients when the boundary layer can't be resolved. Turbulent transfer velocities are higher when evaluated near the ice boundary where u_* is higher and the layer thickness is smaller, i.e. the fluid is closer to the ice boundary and experiences more shear than the fluid that is further from
355   the wall. Shear velocity values range $0.005 - 0.175$ cm/s with the lowest values arising from the zones of slowest flow near the salt-wedge interface. This low shear velocity would place these simulations in the "stratified" or "diffusive-convection" regime identified in Rosevear et al. (2022). The melt rate predicted by the S99 parameterization decreases as the temperature is chosen further from the ice but still within the upper freshwater layer, due to decreasing γ_T. Once within the salt wedge, the predicted melt rate increases due to increased T_w and γ_T from higher seawater velocities. Since γ_T, $\sqrt{C_d}\Gamma_T$, and indirectly $\dot{m}_S$ are
360   functions of u_*, they each tend to zero near the middle of the subglacial environment due to the freshwater outflow interacting with the intrusion inflow, producing a region with zero velocity. Below this, γ_T, $\sqrt{C_d}\Gamma_T$, and $\dot{m}_S$ all increase again, following the velocity profile until the bottom boundary condition is imposed.

    When calculating DC-driven melt rates, the thermal gradients are taken near the ice boundary, ideally over the width of the viscous sublayer, the near-wall portion of the boundary layer where viscous forces dominate. Due to the constraints on
365   resolution and domain, we also test the sensitivity of the diffusive melt framework to various choices of ice distance to obtain ρ_w and $\frac{\partial T}{\partial y}$. Again, we take profiles along the intrusion wedge to evaluate equation 9. Figure 6 B shows the estimates for $\dot{m}_{DC}$ caused by diffusive forced melting from equation 9. As with the S99 parameterization, the highest values for $\dot{m}_{DC}$ arise when seawater properties are taken near the ice boundary, where the largest thermal gradient exists (Figure 3). DC melt rates decrease when the reference point is out of the intrusion and upstream of the subglacial environment, where the water column becomes
370   uniform with fresh, cold glacial runoff.

    Three distinct issues make it difficult to apply existing parameterizations in regions of seawater intrusion: (1) stratification, (2) the interaction of two boundary layers, and (3) change in water flow direction near the ice boundary. Most melt parameterizations assume a well-mixed and fully developed boundary layer, with reference temperature and salinity taken beyond or at the boundary layer's edge. However, in the simulations presented here, there is stratification due to insufficient mixing between
375   the upper layer of subglacial discharge and the lower-layer of seawater intrusion. Intrusion beyond a grounding line entails fluid flow between two boundaries, which is intrinsically different than the geometries considered for other ocean-induced melting regimes (flow bounded by a singular wall on one side). The upper fresh glacial water will have a boundary layer with the ice, and the lower saline ocean water will generate a boundary layer with the bed. In the subglacial environment, the opposing fresh and saline flows meet and create an interfacial boundary with zero velocity. The sharp transition in opposing flows and
380   strong interfacial shear is associated with two accelerating fluid layers that are increasing drag on their respective boundaries. Here, where subglacial environments have thicknesses of 5 or 7.5 cm, and freshwater velocities ranging 5 cm/s to 0.05 cm/s, a complete and stable boundary layer never develops indicating the entire subglacial domain feels the effect of at least one boundary. This means there are multiple transport processes (turbulent and viscous) operating at the same relative importance, rather than one mechanism dominating the other.

4 Discussion

In the context of previous work, these simulations confirm that freshwater flux and the geometry of the subglacial environment are both strong controls on seawater intrusion. Our simulated intrusions follow the general trend and scale sensitivity to those identified in previous laboratory experiments (Figure 7) (grey markers; Wilson et al., 2020) which are within a factor of 10 to the theoretical prediction (dashed line) from Robel et al. (2022). Previous studies estimate possible seawater intrusion distances of kilometers to 10s of kilometers (Wilson et al., 2020; Robel et al., 2022), which give many orders of magnitude difference than any of the intrusions simulated in this study. This difference is likely due to the drag coefficient at the ice wall (C_d), which field studies of ocean flow under sea ice (Mcphee, 1980; Randelhoff et al., 2014; Brenner et al., 2021) and geometric parameterizations (Lu et al., 2011) estimate to be of order 10^{-3} to 10^{-2}. In this study, the drag coefficient of the wall cannot be prescribed but rather is an emergent property arising from the no-slip kinematic boundary condition and momentum dissipation within the model from the $\kappa - \epsilon$ closure scheme. Calculating the drag coefficient using model output gives C_d with values of order 10^{-2} to 10^0. The analytical theory of intrusion distance (L) for an unobstructed water sheet from Robel et al. (2022) is,

$$L = \frac{H^2 g'}{4C_d^2 u_f^2} \tag{10}$$

where $H = 0.05$ m is the height of the subglacial environment, $g' = 0.20$ m/s^2 is the reduced gravity, and C_d is set to the maximum value within the intrusion. Assuming an unobstructed sheet with negligible drag at the salt wedge interface gives a predicted intrusion distance of approximately 5 meters for the intermediate flow case considered in this study (i.e., comparable to the blue lines in Figure 2 A). The theory thus overestimates intrusion distance by about a factor of 2. Better agreement between the theory and model results presented here can be obtained by using averaged ice-parallel velocities within the intrusion and averaged intrusion drag values. One possible explanation for the disagreement is the assumption of negligible interfacial drag. Robel et al. (2022) finds that including interfacial drag of order 10^{-4} reduces predicted intrusion distance by about a factor of 2. Other factors to consider in future development of more realistic theories of seawater intrusion are the potential role of melt feedbacks which we have shown above are important to setting the intrusion dynamics and basal melt rates, and drag from the bottom of the channel which will have different mechanical properties than the ice base. There are two limitations to consider within ANSYS Fluent when melt is enabled: (1) the geometry of the subglacial environment does not change, providing no geometric feedback like that considered in Bradley and Hewitt (2024) and (2) changing the ice wall to a velocity inlet means there is no boundary drag acting on the fluid. Both of these limitations will influence overall intrusion distance, however, we can conclude that the addition of buoyant melt feedback dynamically changes seawater intrusion and affects the overall flux of freshwater which ultimately controls intrusion distance.

Figure 5 demonstrates the disagreements between the melt calculated directly in our high-resolution simulations and the predicted basal melt rates from parameterizations. The S99 parameterization assumes transport of heat and salt is dictated by transfer velocities (γ_T, γ_S). The transfer velocities calculated directly from our simulations are in good agreement with those previously documented (Figure 6, A6). These turbulent transfer velocities are derived from theory and experimental results of pipe flow that assume the fluid is steady and parallel to the wall. In seawater intrusions flow is spatially varying,
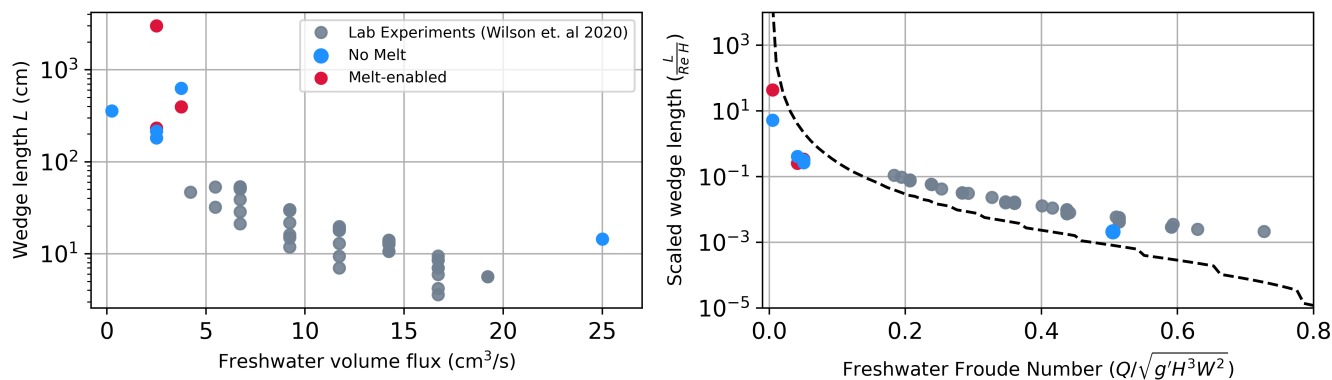
Figure 7. Comparison between Wilson et al. (2020) experimental data (gray markers) and intrusion characteristics found in this study (red and blue markers). The black dashed line is the numerical solution to Robel et al. (2022) with $\gamma = 2$.

with opposing directions of flow parallel to the wall and some flow perpendicular to the wall. The combined effect of low velocities and narrow gaps under grounded ice (we test subglacial domains with 5, 7.5 cm gap height in this study) means

420 that the viscous sublayer and buffer layer together occupy the entire domain considered, and drag from either boundary affects our entire subglacial domain (Figure A10). The turbulent transfer velocities in the S99 parameterization are intended to be used with ocean properties at the edge or beyond the outer boundary layer - if the domain of interest does not develop the full boundary layer then this theory of heat and mass transfer is not appropriate. Since the entire subglacial environment is within the viscous sublayer (where viscous effects dominate) or the buffer layer (where viscous effects and turbulence both occur),

425 the S99 parameterization is not appropriate for described melt from seawater intrusions. This is expected since S99 was not formulated considering domains of seawater intrusion and strong stratification.

If we anticipate viscous effects to dominate in seawater intrusions under grounded ice, then using the thermal and haline molecular diffusivities as so-called "transport velocities" would be appropriate, similar to the diffusive-convective framework presented above. In polar settings where seawater is warmer than subglacial discharge, DDC could be the fitting heat transfer

430 mechanism, acting against the stratification that persists from seawater intrusion. However, this requirement limits this mechanism's relative importance in Antarctica where seawater can be colder than the pressure-dependent freezing point for subglacial discharge (Davis et al., 2023). DDC is dominant where shear is weak, traditionally in low-flow, highly stratified environments, where the geometry does not favor strong natural convection (Rosevear et al., 2021). Observations beneath Ross Ice Shelf near the grounding zone hint at the potential for DDC to contribute to vertical mixing when the water column is structured by an

435 upper layer of cold, fresher adjacent to the ice and a mixed homogenized layer at depth (Begeman et al., 2018). Conceptually, we may expect DDC to be a good description of the source of mixing and basal melt in these simulations (as hypothesized by Robel et al., 2022), given the right oceanographic settings. Due to model limitations, the results presented here do not include melt from salt diffusion, hindering a direct comparison to a DDC parameterization (e.g. eq. B1 in Rosevear et al., 2022). Future

work should prioritize parameterizing this form of ice loss in regions of seawater intrusion using high-resolution models that
440   can resolve the boundary layer structure.

Currently, only Bradley and Hewitt (2024) have considered the problem of intrusion-induced melting and allows the subglacial gap to grow in height due to melting in the region of seawater intrusion. Since a taller subglacial gap leads to further seawater intrusion (as predicted in Wilson et al., 2020; Robel et al., 2022) this geometric effect constitutes a positive feedback on seawater intrusion. Our study includes feedbacks from basal melting on flow within the subglacial environment, but not
445   this geometric feedback. We find that intrusion-induced melt pushes the intrusion interface downward within the subglacial space, dynamically changing the vertical water structure. The increase in stratification and reduction of near-ice thermohaline gradients act to suppress further melting, thus constituting a negative feedback on seawater intrusion. Here, we represented the ocean thermal forcing to the ice by the ice adjacent thermal gradient, as opposed to an average of the water column's temperature as done in Bradley and Hewitt (2024). In this study, there is non-negligible melt for 50% of the intrusion distance, whereas
450   averaging the water column temperature results in melt across the entire intrusion. This latter approach potentially enhances the strength of the geometric feedback over a wider area of the ice. The widening of the subglacial space will compete with the excess buoyant forcing to influence seawater intrusion development. Furthermore, tidal pumping of intrusions will add another scale of complexity in resolving these feedbacks, since they provide a temporally asymmetric melt rate as demonstrated in Gadi et al. (2023). Further work is needed to consider both feedbacks within a single modeling framework to determine which
455   ultimately dominates, and under what conditions since they operate on different temporal and spatial scales.

Due to computational limitations, our simulations cannot span the full range of discharge velocities and geometric sizes of potential seawater intrusion domains. However, the cases considered here are comparable to several cases where subglacial properties are constrained from observations (Carter et al., 2017; Davis et al., 2023; Washam et al., 2020), indicating the need for a parameterization that operates as a function of boundary layer processes, near-ice (order of cms) seawater properties, and
460   buoyant stability of the water column. Scaling the simulations presented here to ice-shelf cavity size domains will limit our ability to resolve boundary layer processes. This scaling issue is not independent of the constraints within large-scale coupled models, where the coarse resolution will not allow for seawater intrusions to form beyond grounding lines. For such coupled models, further experimentation is needed to identify a sub-grid basal melt parameterization (i.e., similar to the purely numerical schemes identified in Seroussi et al., 2019) that can be applied to grounded ice as a function of local bed characteristics,
465   freshwater flux, and thermal forcing. Complex-sloping ice wall boundaries likely couple the seawater intrusion dynamics to the proglacial plume, providing an avenue to combine these processes in a single framework for coupled models with resolution $\mathcal{O}(\text{kms})$.

The challenges associated with complex fluid dynamics and computational limitations are not limited to domains of seawater intrusion. These challenges also apply to the $100's$ of meters downstream of the grounding line where a small vertical gap
470   exists between the ice and seafloor. The transition from a two-wall bounded flow to a single-wall bounded flow influenced by buoyant, shear, and diffusive instabilities is currently not represented in coupled models. It is likely this transition couples plume dynamics to intrusion dynamics which may provide a baseline framework to unify the transition. This regime transition,

475   A sophisticated implementation of seawater intrusion in coarse-grid coupled ice-ocean models is possible. It would require
simulating subglacial hydrology, estimating discharge fluxes, and deducing the required scale at which the ocean grid should
extend under "grounded" glacier ice. From there, a modified basal melt parameterization could be added to calculate an in-
trusion melt rate. If a closed-form parameterization based on first-principles theory is not possible in the complex case of
seawater intrusion, a modified parameterization based on a comprehensive suite of high-resolution CFD simulations, similar

480 to this study, could be used to constrain an effective parameterization. Alternatively, intrusion-induced melt could be included
in a more ad-hoc manner by extending the ocean grid to some prescribed distance inland set by a modified form of the theory
proposed by Robel et al. (2022). A prior ice sheet model intercomparison (Seroussi et al., 2019) study found that when sub-grid
melt schemes are applied to partially floating grid points (cells that cross the grounding line), projected sea level contributions
from the Antarctic ice sheet can be up to twice as high. Such sub-grid melt schemes have a similar effect to intrusion-induced

485 basal melt.

5   Conclusions

Seawater intrusion beneath grounded portions of ice sheets leads to complex interactions between the subglacial hydrologic
system and the ocean. The ability for seawater to intrude under grounded ice is dependent on the subglacial discharge velocity
and geometry of the subglacial environment. Both of these controls are consistent with studies of estuaries (Krvavica et al.,

490 2016), bolstering the idea that grounding zones are subglacial estuaries (Horgan et al., 2013). Here, we found that intrusion-
induced basal melting dynamically alters the intrusion, constituting a negative feedback that will compete with the geometric
positive feedback identified in another study (Bradley and Hewitt, 2024). Our simulations show that seawater intrusion can
produce enhanced melting at, and just upstream of, the grounding line where warm seawater occupies most of the subglacial
environment, with melt rates on the order of 10's of meters per year for the configurations considered in this study. Current basal

495 melt parameterizations that assume a fully-developed boundary layer underpredict basal melt rates due to seawater intrusion by
more than an order of magnitude. Diffusive melting frameworks do a better job of estimating intrusion-induced basal melt near
the grounding line where melt rates are high, however, further upstream this framework also fails. For DDC-driven melting to
occur, the seawater has to be warmer than the subglacial discharge, which we expect to limit its applicability in Antarctica.
Theories of heat and salt transfer that consider the complex overlap of transport phenomena occurring in the buffer layer should

500 be further considered to better incorporate basal melt from seawater intrusion in coarse models.

    Coupled ice-ocean models do a poor job of reproducing observed patterns of enhanced basal melt near grounding lines due
to resolution and the assumptions inherent in melt parameterizations (Adusumilli, 2021; Ciracì et al., 2023). Furthermore, the
assumption of a hydraulic barrier between subglacial hydrology and the ocean leads to an incomplete consideration of the fluid
dynamics at grounding zones. Improving projections of the ice sheet contributions to sea level rise requires a more complete

505 representation of grounding zones as dynamic estuaries where subglacial hydrology, the ocean, and glacier ice all interact.

Appendix A: Methods

Variable	Description	Value	Units	Equation
L_i	Latent heat	334000	J/kg	
c_w	Seawater heat capacity	4011.4	J/kgC	
ρ_w	Seawater density		kg/m^3	1
S_w	Seawater salinity		ppt	
T_w	Seawater Temperature		C	
S_f	Subglacial discharge salinity	0	ppt	
T_f	Subglacial discharge Temperature	0	C	
S_o	Seawater inlet salinity	30	ppt	
T_o	Seawater inlet Temperature	0.5	C	
μ_t	Eddy viscosity		m^2/s	2
C_μ	Turbulence modulation			
κ_T	Thermal Conductivity of seawater	0.57	W/mC	
ϵ	Eddy dissipation		m^2/s^3	
κ	Turbulent kinetic energy		m^2/s^2	
C_d	Drag coefficient			3
u_*	Shear velocity		m/s	8
u	Freestream fluid velocity		m/s	
$\dot{m}$	Modeled melt rate		m/s	4
ρ_i	Ice density	918	kg/m^3	
T_i	Ice-ocean interfacial temperature	0	C	
S_i	Ice-ocean interfacial salinity	0	ppt	
N^2	Buoyancy Frequency		s^{-2}	5
g	Gravitational Constant	9.81	m/s^2	
ρ_0	Reference density	1000	kg/m^3	
$\dot{m}_S$	Parameterized shear melt rate		m/s	6
γ_T	Thermal Turbulent transfer velocity		m/s	7
γ_S	Haline Turbulent transfer velocity		m/s	
$\Gamma_T\sqrt{C_d}$	Thermal Stanton Number			

c_i	Heat capacity of ice	2009	J/kgC	
κ_i	Thermal conductivity of ice	2.22	W/mC	
$\partial T_i/\partial y$	Vertical ice thermal gradient	0	C/m	
Pr	Prandtl Number	13.8		
ν	Kinematic viscosity of seawater	$1.95*10^{-6}$	m^2/s	
u_f	Subglacial discharge velocity	$5, 0.5, 0.05$	cm/s	
u_o	Seawater velocity	0.5	cm/s	
K_T	Thermal molecular diffusivity	$1.4*10^{-7}$	m^2/s	
$\dot{m}_{DC}$	Parameterized double-diffusive melt rate		m/s	9
g'	Reduced gravitational constant	0.22	m/s^2	
H	Height of subglacial space	$5, 7.5$	cm	
H_c	Height of near-ice grid cell		m	
θ	Slope of subglacial space	$0.5, 1$	$c°$	
L	Theoretical intrusion distance		m	10

Table A1: Variable descriptions and values

A1 Domain

The 2-dimensional domain is defined as a long and thin subglacial environment attached to a tall rectangular ocean basin. The length of the subglacial environment is 30 m for all cases. The height of the subglacial domain is 5 cm for all cases except the thicker scenario where the height is 7.5 cm. The tank's height is 5 m and its width is 2 m for all cases. For analysis, we designate the 'grounding line' or the point where the subglacial environment meets the ocean basin to be at $x = 0$ m. However, in the model domain, this point exists at $x = 2$ m.

A freshwater inlet is defined at the rightmost boundary of the subglacial environment. An ocean water inlet is defined at the leftmost boundary. A pressure outlet is set at the top of the ocean domain, enforcing a no-gradient flux across the boundary. The ice boundary walls are defined at the top of the subglacial environment and the right side of the ocean domain. For non-melt-enabled cases, these ice walls have a defined boundary temperature requirement at 0 deg C with no salinity diffusion. For melt-enabled cases only the top boundary of the subglacial space is turned into a velocity inlet to simulate melt. We do this to isolate the added buoyancy flux to only intrusion-induced melt and not vertical plume dynamics that would arise from the vertical ice boundary.

A2 Meshing

For the given turbulence closure scheme employed here (low Reynolds k-e turbulence model) a nondimensionalized distance, $y+$, must be $<= 5$. This follows the law-of-the-wall principle, where mesh thickness near the wall must be coordinated with

$u_f[cm/s]$	$u_o[cm/s]$	C_μ	melting	$H[c]$	θ
5	0.5	0.18	off	5	0
5	0.5	0.09	off	5	0
5	0.5	0.045	off	5	0
5	0.5	0.09	on	5	0
0.5	0.5	0.18	off	5	0
0.5	0.5	0.09	off	5	0
0.5	0.5	0.045	off	5	0
0.5	0.5	0.09	on	5	0
0.05	0.5	0.18	off	5	0
0.05	0.5	0.09	off	5	0
0.05	0.5	0.045	off	5	0
0.05	0.5	0.09	on	5	0
0.05	5	0.09	off	5	0
0.5	0.5	0.09	off	5	1
0.5	0.5	0.09	off	5	0.5
0.5	0.5	0.09	on	5	0.5
0.5	0.5	0.09	off	7.5	0
0.5	0.5	0.09	on	7.5	0

Table A2. All runs conducted in ANSYS Fluent

the closure scheme for near-wall viscosity effects to be rendered correctly. This nondimensionalized distance y+ is a function of dynamic viscosity, density, distance normal to the wall, and shear velocity.

$$y^+ = \frac{u_* y \rho_w}{\mu} \tag{A1}$$

Given a value for y+, $\mu = 1.7E - 03$ kg/ms for dynamic viscosity, and seawater density $\rho_w = 1020$ kg/m^3, all that is needed
530   is the shear velocity, u_* in order to find the necessary dimensional y distance of the first grid cell. To find u_* we need the skin friction C_f. For laminar flows, the skin friction is:

$$C_f = \frac{16}{Re} \tag{A2}$$

Where Re is the Reynolds number with the characteristic length being the channel length :

$$Re_x = \frac{uL\rho_w}{\mu} \tag{A3}$$

535   To find u_*:

$$u_* = \sqrt{\frac{\tau}{\rho_w}} \tag{A4}$$

Where $\tau = \frac{1}{2}\rho C_f u^2$. Rearranging we then get:

$$u_* = \sqrt{\frac{1}{2}C_f u^2} \tag{A5}$$

We can then plug this value for u_* back into A1 equation to calculate the near-wall mesh thickness.

540 **A3   Run-Time**

To keep the simulation time consistent, each simulation runs for $43,200s$ ($12hrs$). Pre and post-runs were conducted to evaluate the steady-state solver solution to the transient solver solution. Those results are discussed further in Fluent Settings.

To set the time step we used the eddy turnover time. This is the largest time step we can take without causing non-physical effects and is represented by the:

545    $$t = \frac{h}{u_*} \tag{A6}$$

where h is the height of the channel. For each simulation, a time-step of $5s$ was chosen in accordance with the fastest freshwater flow (in turn has the largest shear velocity, and therefore smallest eddy turnover time). Putting this together, for all runs, a total of $86,400$ time steps were taken at a time step of $5s$. For every $20th$ time step ($100s$) data was exported along a middle transect, the ice base, and the domain's fluid surface.

550 **A4   Fluent Settings**

We employed the low-re k-e turbulence closure model to allow for increased resolution near the ice boundaries. This formulation of the k-e turbulence model employs damping equations that allows it to resolve the viscous sublayer and as such the complete boundary layer structure. We tested this against the enhanced wall treatment formulation of the k-e model that resolves the viscous boundary layer by a two-layer approach defining the wall-adjacent region as a viscous zone and the rest as
555   an outer turbulent layer. This two-layer approach is smoothly blended into the freestream solution that employs the standard k-e model. The results presented in the main body of this work employ the low-re formulation, however, we note that intrusion distance can change based on the choice of turbulence closure formulation. This is distinctly different than the amount of turbulence negligibly changing the intrusion distance as we discuss in the results section of the main text. Different closure schemes will resolve the flow structure differently, leading to a nominal change in intrusion distance, but changing the amount
560   of turbulence in a given turbulence closure scheme does not largely affect intrusion distance.

The k-e turbulence model provides a simple pathway to modulate the amount of turbulent mixing, by changing the C_μ value. The C_μ value controls the amount of relative turbulent kinetic energy to dissipation represented in the eddy viscosity value and thus the Reynolds stresses via the buossinesq hypothesis.

To simulate the effects salinity and temperature have on fluid density, we employed the species transport model with a user-defined equation based on a linear equation of state for seawater (eq. 1). This linear equation of state prohibits any cabling or baroclinicity effects. Need to list reference values, materials info, the methods and controls.

Fluent automatically turns on energy conservation when species transport is enabled and solves for water temperature via:

$$\frac{\partial}{\partial t}(\rho_w E) + \nabla(v(\rho_w E + p)) = \nabla(k_{eff}\nabla T - \Sigma)jh_j J_j + (\tau_{eff}\dot{v})) + S_h. \tag{A7}$$

The first three terms on the right-hand side represent energy transfer due to the conduction of heat, species diffusion, and, molecular dissipation, respectively. S_h represents chemical sources of heat; here, there are none so this term is zero (ANSYS, 2009). The left-hand side represents the time evolution of energy and energy advection. This energy transport equation also represents the transport of temperature throughout the domain, with the relation $T c_w \rho_w V = E$, where T is temperature, c_w is the heat capacity, ρ_w is the seawater density, and V is the volume.

The results presented in the main body of this work are the time-averaged results from the transient run of 12 hrs. A series of tests were conducted to evaluate Fluent's steady-state solver to the transient solver and their corresponding solutions. The domain is initialized with a saline, warm ocean tank and a fresh, cold subglacial environment with no intrusion. We run the steady-state with this initialization (named steady state pre), and in most cases, a small intrusion develops and occasionally no intrusion. A secondary steady-state is run after the intrusion develops in the transient solver, using the transient solution as the initial condition (named steady state post). In the post steady-state run, the intrusion developed during the transient simulation stays steady and persists. Therefore, the steady-state solver is sensitive to the initial condition provided and we thus disregard the steady state pre results. To compare the steady state post and transient solutions, we plot the intrusion distances against each other, in which they neatly collapse on a 1 to 1 line.

A5 Variable Ocean Forcing

Preliminary work demonstrated little to no dependence on intrusion distance due to seawater velocity. The change in intrusion distance from an order of magnitude difference in ocean velocity was much smaller than a change in intrusion distance due to an order of magnitude difference in the freshwater discharge velocity.

A6 Retrograde Slopes

We tested two retrograde slopes, $\theta = 0.5°, 1°$. The former slope is the condition presented in the main body of this work, where the intrusion was reduced. However, the $1°$ slope did increase intrusion distance. Disentangling this relationship will require further work.
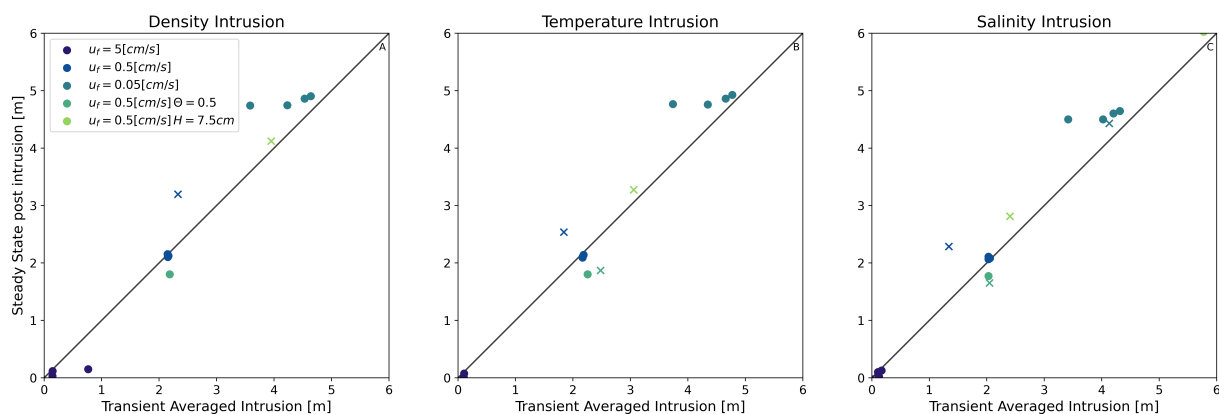
Figure A1. Comparison of seawater intrusion distances for ANSYS Fluent's steady-state vs transient solver. Intrusion distances are based on density, salinity, and temperature criteria.
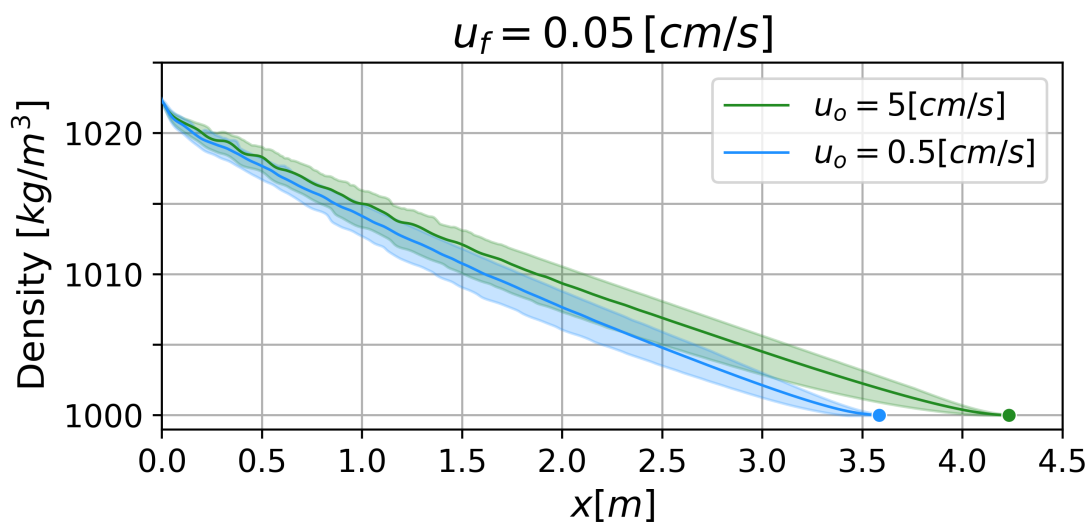
Figure A2. Testing two different seawater velocities (u_o) on intrusion distance for the slowest freshwater case ($u_f = 0.05$ cm/s). The blue line represents the standard u_o tested in the rest of this study, and the green line represents an order of magnitude difference.
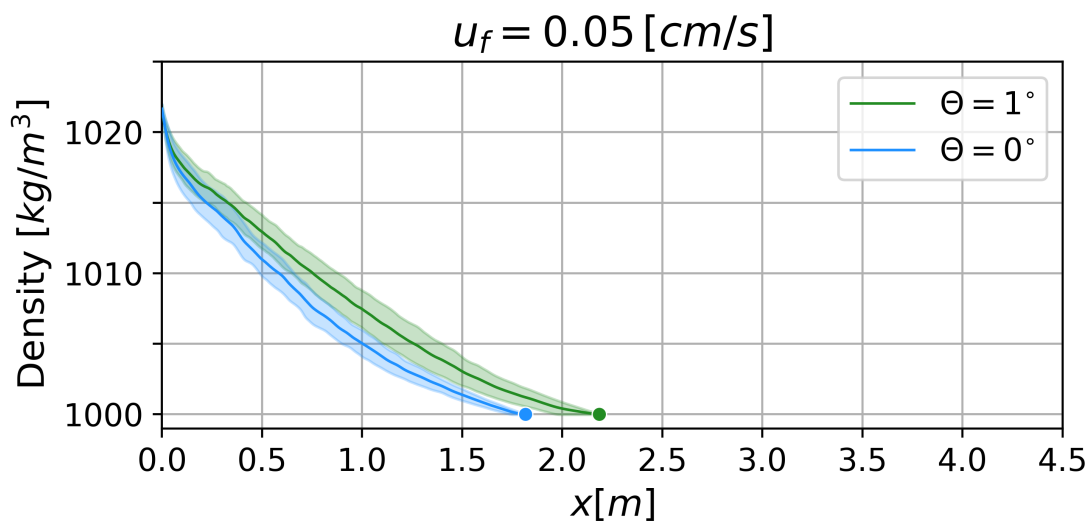
Figure A3. Testing two different retrograde slopes. The blue line is the slope representative of the condition presented in the main text and the green line is a doubling of this slope. Shading represents the first temporal standard deviation.
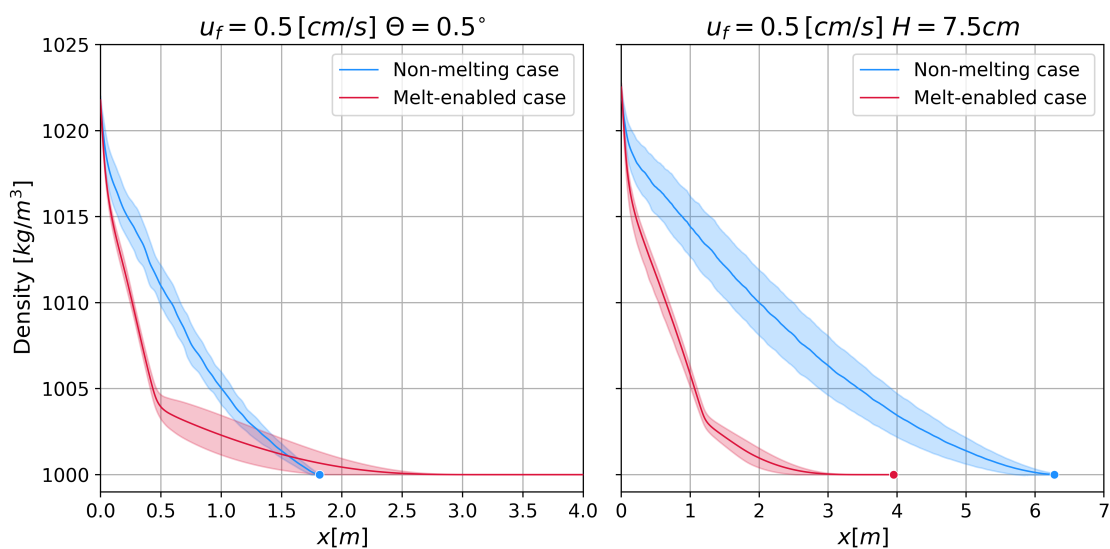
Figure A4. Seawater intrusions for the retrograde and thicker domains. Red lines are for melt-enabled scenarios and blue lines are for non-melt enabled.
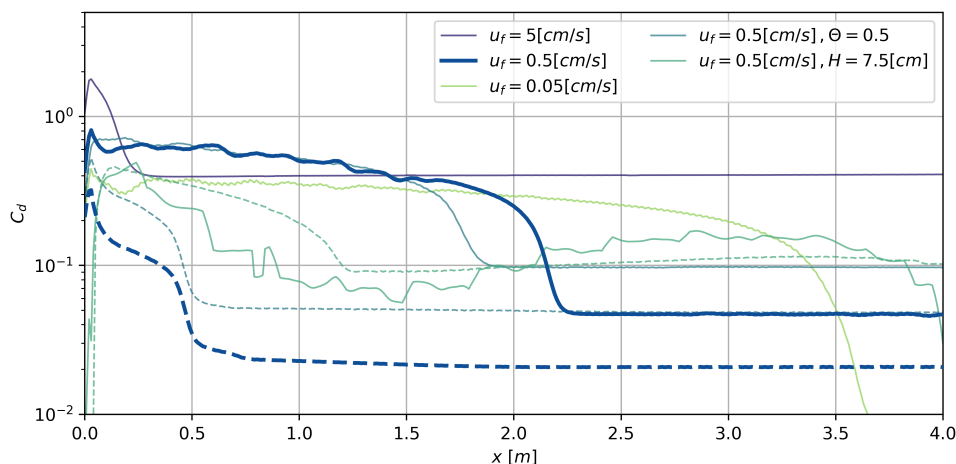
Figure A5. Drag coefficients for all cases tested. Solid lines are non-melt enabled cases. Dashed lines are melt-enabled.

A7 Melt-Enabled Cases for Retrograde and Thicker Domains

A8 Drag Coefficients

Within this modeling framework, drag is not prescribed, but rather diagnosed from the model output. We use the relationship given by 3 to relate the drag coefficient to the near-ice velocity gradient. We find drag coefficients in the range of 10^{-2} to

595   10^0, higher than values typically used in models or observed in the field. This drag coefficient does increase over the region of seawater intrusion, tending to a smaller background value upstream of the intrusion. For all melt-enabled cases tested, the drag coefficient decreases. However, this is most likely due to changes to the kinematic boundary condition than a physically meaningful reduction.

A9 Haline Stanton Number

600   Because our melting model does not consider any effects from dissolution, we ignore the contribution to melting from salt in the direct comparison. However, with the model output we can obtain a haline turbulent transfer velocity and a haline Stanton number similar to equation 7. The haline stanton number is in good agreement with previously published values.

A10 Plume Results

Although not investigated within this work, to verify the physics of the fluid domain are operating correctly, we looked at plume

605   development within the ocean tank. In every case, a plume develops, however, the velocity of the plume varies depending on the freshwater discharge rate. This is in accordance with current literature, and we anticipate intrusion-plume dynamics to be inextricably linked.
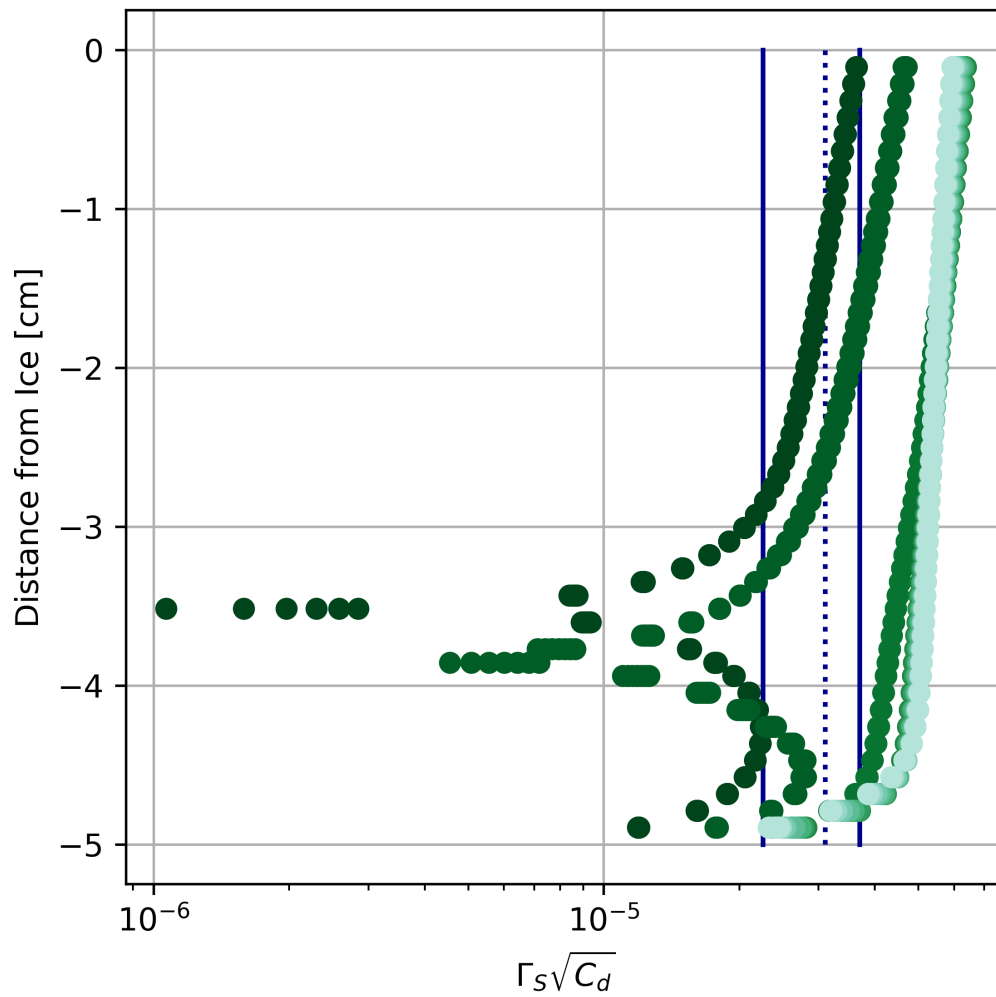
Figure A6. Haline Stanton Number for $u_f = 0.5$ cm/s and medium turbulence. The blue lines represent previously published thermal Stanton numbers. The dotted is Jenkins et al. (2010) and the solid from Washam et al. (2023).
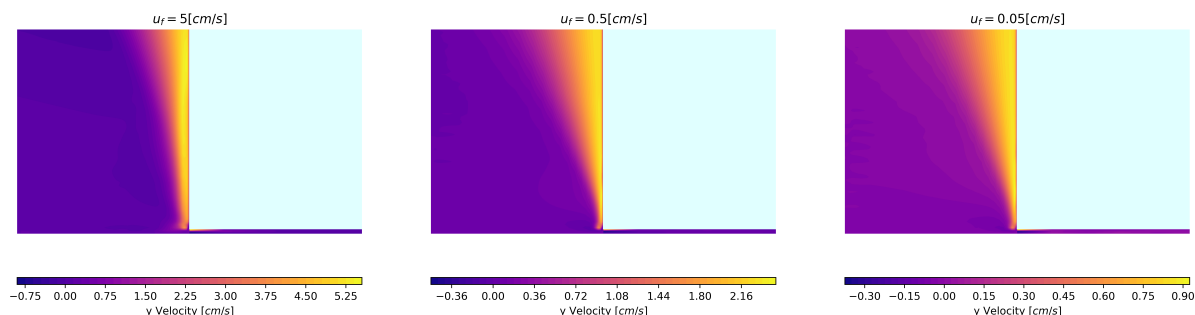
Figure A7. vertical velocity component in cm/s for all three freshwater velocity cases ($u_f = 5, 0.5, 0.05$ cm/s) and medium turbulence ($C_\mu = 0.09$). Note the plume structure that rises along the ice face.

A11 Vertical Profiles

Author contributions. A.A.R., E.W., C.C.K.L, and M.M. conceived the presented work and methodology. M.M. conducted all simulations
610   and analyses. A.A.R. aided in the simulation set-up and analysis. C.C.K.L. provided consultation on the methods and background theory.
P.W. and E.W. contributed to interpreting the analysis and choosing the appropriate melt parameterization schemes to test. A.A.R. supervised
the findings of this work. M.M. wrote the manuscript with assistance from A.A.R. and consultation with C.C.K.L, E.W., and P.W. .

Competing interests. The authors declare that they have no conflict of interest.

Acknowledgements. We acknowledge the computing resources that made this work possible provided by the Partnership for an Advanced
615   Computing Environment (PACE) at Georgia Tech in Atlanta, GA. We would like to thank research scientist Fang (Cherry) Liu for her
assistance on challenges related to PACE and HPC. Financial support for this work came from startup funding from Georgia Tech and the
University System of Georgia.
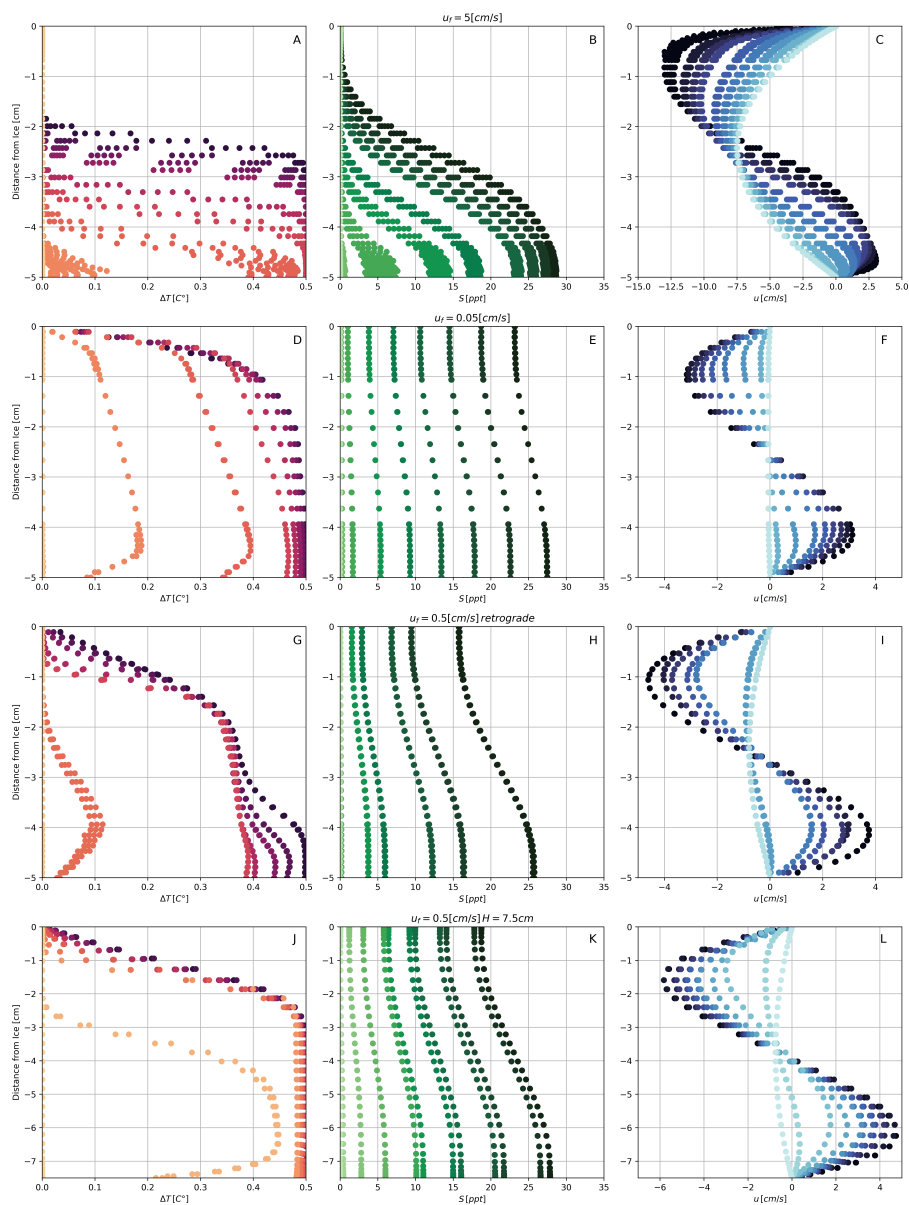
Figure A8. Profiles of temperature (first column), salinity (middle column), and x-component of velocity (last column) for non-melt cases with medium turbulence. Panels A-C is for $u_f = 5$ cm/s, D-F is for $u_f = 0.05$ cm/s, G-I is for $u_f = 0.5$ cm/s with a retrograde slope, and J-L is for $u_f = 0.5$ cm/s with a thicker subglacial environment where the height is 7.5 cm.
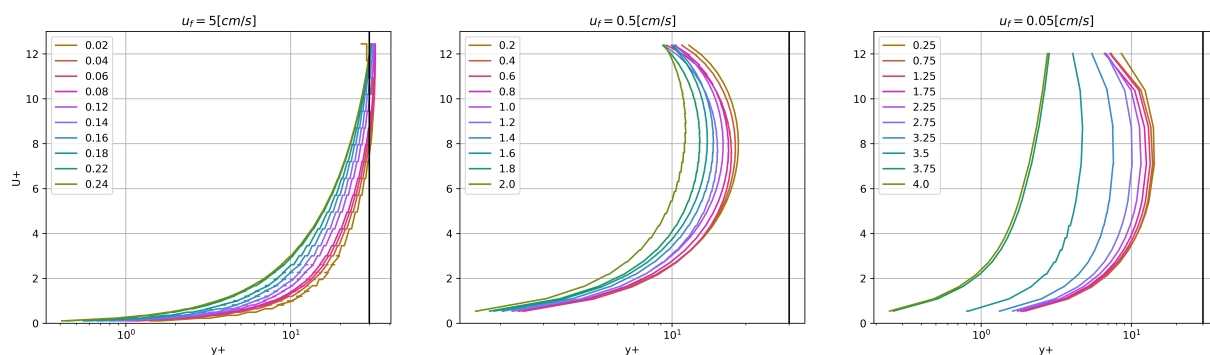
Figure A9. Law of the wall for standard geometry cases, medium turbulence, all velocities.
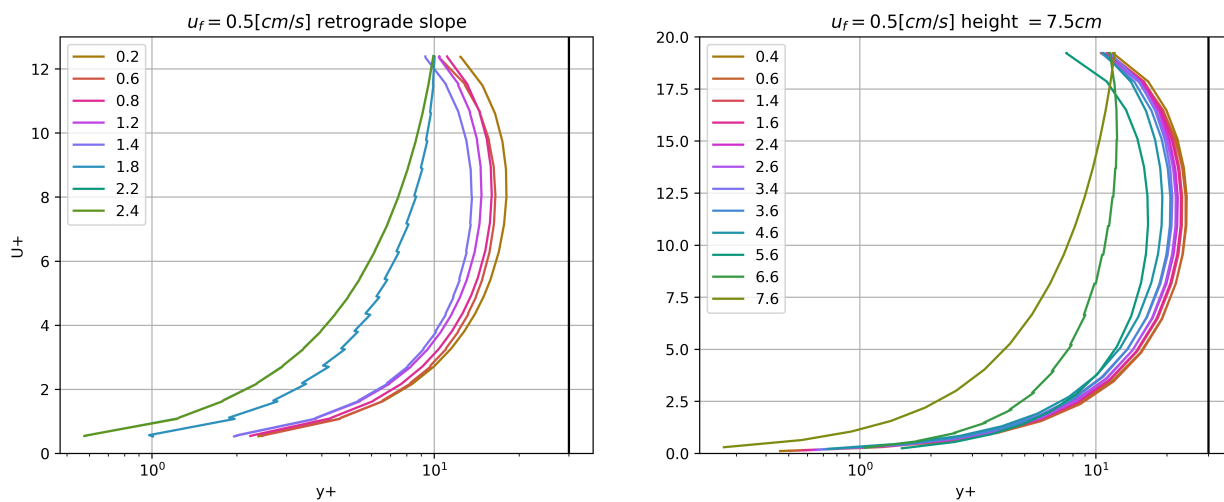
Figure A10. Law of the wall for the alternate geometry cases, medium turbulence, freshwater velocity $u_f = 0.5$ cm/s.

References

Adusumilli, S.: Satellite observations of atmosphere-ice-ocean interactions around Antarctica, 2021.

620 ANSYS: ANSYS Fluent 12.0 User's Guide, https://www.afs.enea.it/project/neptunius/docs/fluent/html/ug/main_pre.htm, 2009.

ANSYS: ANSYS Fluent - CFD Software | ANSYS, http://www.ansys.com/products/fluids/ansys-fluent, 2022.

Begeman, C. B., Tulaczyk, S. M., Marsh, O. J., Mikucki, J. A., Stanton, T. P., Hodson, T. O., Siegfried, M. R., Powell, R. D., Christianson, K., and King, M. A.: Ocean Stratification and Low Melt Rates at the Ross Ice Shelf Grounding Zone, J. Geophys. Res.-Oceans, 123, 7438–7452, https://doi.org/10.1029/2018JC013987, 2018.

625 Bradley, A. T. and Hewitt, I. J.: Tipping point in ice-sheet grounding-zone melting due to ocean water intrusion, Nat. Geosci., https://doi.org/10.21203/rs.3.rs-2924707/v1, 2024.

Brenner, S., Rainville, L., Thomson, J., Cole, S., and Lee, C.: Comparing Observations and Parameterizations of Ice-Ocean Drag Through an Annual Cycle Across the Beaufort Sea, J. Geophys. Res.-Oceans, 126, https://doi.org/10.1029/2020JC016977, 2021.

Carter, S. P., Fricker, H. A., and Siegfried, M. R.: Antarctic subglacial lakes drain through sediment-floored canals: Theory and model testing
630 on real and idealized domains, The Cryosphere, 11, 381–405, https://doi.org/10.5194/tc-11-381-2017, 2017.

Christianson, K., Bushuk, M., Dutrieux, P., Parizek, B. R., Joughin, I. R., Alley, R. B., Shean, D. E., Abrahamsen, E. P., Anandakrish-nan, S., Heywood, K. J., Kim, T. W., Lee, S. H., Nicholls, K., Stanton, T., Truffer, M., Webber, B. G., Jenkins, A., Jacobs, S., Bind-schadler, R., and Holland, D. M.: Sensitivity of Pine Island Glacier to observed ocean forcing, Geophys. Res. Lett., 43, 10,817–10,825, https://doi.org/10.1002/2016GL070500, 2016.

635 Ciracì, E., Rignot, E., Scheuchl, B. I., Tolpekin, V. I., Wollersheim, M., An, L., Milillo, P., Bueso-Bello, J.-L. I., Rizzoli, P. I., Dini, L., by R Byron Parizek, and Robel, A. A.: Melt rates in the kilometer-size grounding zone of Petermann Glacier, Greenland, before and during a retreat, P. Natl. Acad. Sci. USA, 120, e2220924 120, https://doi.org/10.1073/pnas, 2023.

Cowton, T., Slater, D., Sole, A., Goldberg, D., and Nienow, P.: Modeling the impact of glacial runoff on fjord circulation and submarine melt rate using a new subgrid-scale parameterization for glacial plumes, J. Geophys. Res.-Oceans, 120, 796–812,
640 https://doi.org/10.1002/2014JC010324, 2015.

Davis, P. E. D., Nicholls, K. W., Holland, D. M., Schmidt, B. E., Washam, P., Riverman, K. L., Arthern, R. J., Vaňková, I., Eayrs, C., Smith, J. A., Anker, P. G. D., Mullen, A. D., Dichek, D., Lawrence, J. D., Meister, M. M., Clyne, E., Basinski-Ferris, A., Rignot, E., Queste, B. Y., Boehme, L., Heywood, K. J., Anandakrishnan, S., and Makinson, K.: Suppressed basal melting in the eastern Thwaites Glacier grounding zone, Nature, 614, 479–485, https://doi.org/10.1038/s41586-022-05586-0, 2023.

645 Depoorter, M. A., Bamber, J. L., Griggs, J. A., Lenaerts, J. T., Ligtenberg, S. R., Broeke, M. R. V. D., and Moholdt, G.: Calving fluxes and basal melt rates of Antarctic ice shelves, Nature, 502, 89–92, https://doi.org/10.1038/nature12567, 2013.

Gadi, R., Rignot, E., and Menemenlis, D.: Modeling Ice Melt Rates From Seawater Intrusions in the Grounding Zone of Petermann Gletscher, Greenland, Geophys. Res. Lett., 50, e2023GL105 869, https://doi.org/10.1029/2023GL105869, 2023.

Holland, D. M. and Jenkins, A.: Modeling Thermodynamic Ice-Ocean Interactions at the Base of an Ice Shelf, Amer. Meteor. Soc., 29,
650 1787–1800, 1999.

Horgan, H. J., Alley, R. B., Christianson, K., Jacobel, R. W., Anandakrishnan, S., Muto, A., Beem, L. H., and Siegfried, M. R.: Estuaries beneath ice sheets, Geology, 41, 1159–1162, https://doi.org/10.1130/G34654.1, 2013.

Hrenya, C. M., Bolio, E. J., Chakrabarti, D., and Sinclair, J. L.: Comparison of Low Reynolds Number k-e Turbulence Models in Predicting Fully Developed Pipe Flow, Chem. Eng. Sci., 50, 1923–1941, 1995.

655   Jackson, R. H., Shroyer, E. L., Nash, J. D., Sutherland, D. A., Carroll, D., Fried, M. J., Catania, G. A., Bartholomaus, T. C., and Stearns, L. A.:
      Near-glacier surveying of a subglacial discharge plume: Implications for plume parameterizations, Geophys. Res. Lett., 44, 6886–6894,
      https://doi.org/10.1002/2017GL073602, 2017.

      Jenkins, A.: Convection-driven melting near the grounding lines of ice shelves and tidewater glaciers, J. Phys. Oceanogr., 41, 2279–2294,
      https://doi.org/10.1175/JPO-D-11-03.1, 2011.

660   Jenkins, A., Nicholls, K. W., and Corr, H. F.: Observation and parameterization of ablation at the base of Ronne Ice Ahelf, Antarctica, J.
      Phys. Oceanogr., 40, 2298–2312, https://doi.org/10.1175/2010JPO4317.1, 2010.

      Kader, B. A. and Yaglom, A. M.: Heat and Mass Transfer Laws for Fully Turbulent Wall Flows, Int. J. Heat Mass Transfer, 15, 2329–2351,
      1972.

      Kim, J. H., Rignot, E., Holland, D., and Holland, D.: Seawater Intrusion at the Grounding Line of Jakobshavn Isbræ, Greenland, From
665   Terrestrial Radar Interferometry, Geophys. Res. Lett., 51, e2023GL106 181, https://doi.org/10.1029/2023GL106181, 2024.

      Kimura, S., Nicholls, K. W., and Venables, E.: Estimation of ice shelf melt rate in the presence of a thermohaline staircase, J. Phys. Oceanogr.,
      45, 133–148, https://doi.org/10.1175/JPO-D-14-0106.1, 2015.

      Krvavica, N., Travaš, V., and Ožanić, N.: A field study of interfacial friction and entrainment in a microtidal salt-wedge estuary, Environ.
      Fluid Mech., 16, 1223–1246, https://doi.org/10.1007/s10652-016-9480-1, 2016.

670   Launder, B. and Spalding, D.: Numerical Prediction of Flow, Heat Transfer, Turbulence and Combustion, Pergamon,
      https://doi.org/https://doi.org/10.1016/B978-0-08-030937-8.50016-7, 1983.

      Lu, P., Li, Z., Cheng, B., and Leppäranta, M.: A parameterization of the ice-ocean drag coefficient, J. Geophys. Res- Oceans, 116,
      https://doi.org/10.1029/2010JC006878, 2011.

      Macgregor, J. A., Anandakrishnan, S., Catania, G. A., and Winebrenner, D. P.: The grounding zone of the Ross Ice Shelf, West Antarctica,
675   from ice-penetrating radar, J. Glaciol., 57, 917–928, https://doi.org/10.3189/002214311798043780, 2011.

      Mansour, N. N., Kim, J., and Moin, P.: Near-wall k-ϵ turbulence modeling, AIAA Journal, 27, 1068–1073, https://doi.org/10.2514/3.10222,
      1989.

      McConnochie, C. D. and Kerr, R. C.: Testing a common ice-ocean parameterization with laboratory experiments, J. Geophys. Res.-Oceans,
      122, 5905–5915, https://doi.org/10.1002/2017JC012918, 2017.

680   McPhee, M.: Air-Ice-Ocean Interaction Turbulent Boundary Layer Exchange Processes, Springer, New York, NY, https://doi.org/10.1007/
      978-0-387-78335-2_5, 2008.

      McPhee, M. G.: The Effect of the Oceanic Boundary Layer on the Mean Drift of Pack Ice: Application of a Simple Model, J. of Phys.
      Oceanogr., 9, 388–400, https://doi.org/https://doi.org/10.1175/1520-0485(1979)009<0388:TEOTOB>2.0.CO;2, 1979.

      Mcphee, M. G.: An Analysis of Pack Ice Drift in Summer, Sea ice processes and models: proceedings of the Arctic Ice Dynamics Joint
685   Experiment International Commission of Snow and Ice symposium, pp. 62–75, 1980.

      McPhee, M. G., Maykut, G. A., and Morison, J. H.: Dynamics and thermodynamics of the ice/upper ocean system in the marginal ice zone
      of the Greenland Sea, J. Geophys. Res.-Oceans, 92, 7017–7031, https://doi.org/10.1029/JC092iC07p07017, 1987.

      Middleton, L., Davis, P. E., Taylor, J. R., and Nicholls, K. W.: Double Diffusion As a Driver of Turbulence in the Stratified Boundary Layer
      Beneath George VI Ice Shelf, Geophys. Res. Lett., 49, e2021GL096 119, https://doi.org/10.1029/2021GL096119, 2022.

690   Milillo, P., Rignot, E., Rizzoli, P., Scheuchl, B., Mouginot, J., Bueso-Bello, J., and Prats-Iraola, P.: Heterogeneous retreat and ice melt of
      Thwaites Glacier, West Antarctica, Sci. Adv., 5, https://doi.org/10.1126/sciadv.aau3433, 2019.

Otosaka, I. N., Shepherd, A., Ivins, E. R., Schlegel, N. J., Amory, C., Broeke, M. R. V. D., Horwath, M., Joughin, I., King, M. D., Krinner, G., Nowicki, S., Payne, A. J., Rignot, E., Scambos, T., Simon, K. M., Smith, B. E., Sørensen, L. S., Velicogna, I., Whitehouse, P. L., Geruo, A., Agosta, C., Ahlstrøm, A. P., Blazquez, A., Colgan, W., Engdahl, M. E., Fettweis, X., Forsberg, R., Gallée, H., Gardner, A., Gilbert, L.,
695   Gourmelen, N., Groh, A., Gunter, B. C., Harig, C., Helm, V., Khan, S. A., Kittel, C., Konrad, H., Langen, P. L., Lecavalier, B. S., Liang, C. C., Loomis, B. D., McMillan, M., Melini, D., Mernild, S. H., Mottram, R., Mouginot, J., Nilsson, J., Noël, B., Pattle, M. E., Peltier, W. R., Pie, N., Roca, M., Sasgen, I., Save, H. V., Seo, K. W., Scheuchl, B., Schrama, E. J., Schröder, L., Simonsen, S. B., Slater, T., Spada, G., Sutterley, T. C., Vishwakarma, B. D., Wessem, J. M. V., Wiese, D., Wal, W. V. D., and Wouters, B.: Mass balance of the Greenland and Antarctic ice sheets from 1992 to 2020, Earth Syst. Sci. Data, 15, 1597–1616, https://doi.org/10.5194/essd-15-1597-2023, 2023.

700   Randelhoff, A., Sundfjord, A., and Renner, A. H.: Effects of a shallow pycnocline and surface meltwater on sea ice-ocean drag and turbulent heat flux, J. Phys. Oceanogr., 44, 2176–2190, https://doi.org/10.1175/JPO-D-13-0231.1, 2014.

Rignot, E., Jacobs, S., Mouginot, J., and B, S.: Ice-Shelf Melting Around Antarctica, Sci., 341, 266–270, https://doi.org/10.1126/science.1235798, 2013.

Robel, A. A., Wilson, E., and Seroussi, H.: Layered seawater intrusion and melt under grounded ice, The Cryosphere, 16, 451–469,
705   https://doi.org/10.5194/tc-16-451-2022, 2022.

Roquet, F., Madec, G., Brodeau, L., and Nycander, J.: Defining a simplified yet "Realistic" equation of state for seawater, J. Phys. Oceanogr., 45, 2564–2579, https://doi.org/10.1175/JPO-D-15-0080.1, 2015.

Rosevear, M. G., Gayen, B., and Galton-Fenzi, B. K.: The role of double-diffusive convection in basal melting of Antarctic ice shelves, P. Natl. Acad. Sci., 118, https://doi.org/10.1073/pnas.2007541118/, 2021.

710   Rosevear, M. G., Gayen, B., and Galton-Fenzi, B. K.: Regimes and Transitions in the Basal Melting of Antarctic Ice Shelves, J. Phys. Oceanogr., 52, 2589–2608, https://doi.org/10.1175/jpo-d-21-0317.1, 2022.

Sayag, R. and Worster, M. G.: Elastic dynamics and tidal migration of grounding lines modify subglacial lubrication and melting, Geophys. Res. Lett., 40, 5877–5881, https://doi.org/10.1002/2013GL057942, 2013.

Schlichting, H. and Gersten, K.: Boundary-Layer Theory, Springer Berlin Heidelberg, https://doi.org/10.1007/978-3-662-52919-5, 2016.

715   Schmidt, B. E., Washam, P., Davis, P. E., Nicholls, K. W., Holland, D. M., Lawrence, J. D., Riverman, K. L., Smith, J. A., Spears, A., Dichek, D. J., Mullen, A. D., Clyne, E., Yeager, B., Anker, P., Meister, M. R., Hurwitz, B. C., Quartini, E. S., Bryson, F. E., Basinski-Ferris, A., Thomas, C., Wake, J., Vaughan, D. G., Anandakrishnan, S., Rignot, E., Paden, J., and Makinson, K.: Heterogeneous melting near the Thwaites Glacier grounding line, Nature, 614, 471–478, https://doi.org/10.1038/s41586-022-05691-0, 2023.

Seroussi, H., Nowicki, S., Simon, E., Abe-Ouchi, A., Albrecht, T., Brondex, J., Cornford, S., Dumas, C., Gillet-Chaulet, F., Goelzer, H.,
720   Golledge, N. R., Gregory, J. M., Greve, R., Hoffman, M. J., Humbert, A., Huybrechts, P., Kleiner, T., Larour, E., Leguy, G., Lipscomb, W. H., Lowry, D., Mengel, M., Morlighem, M., Pattyn, F., Payne, A. J., Pollard, D., Price, S. F., Quiquet, A., Reerink, T. J., Reese, R., Rodehacke, C. B., Schlegel, N. J., Shepherd, A., Sun, S., Sutter, J., Breedam, J. V., Wal, R. S. V. D., Winkelmann, R., and Zhang, T.: InitMIP-Antarctica: An ice sheet model initialization experiment of ISMIP6, The Cryosphere, 13, 1441–1471, https://doi.org/10.5194/tc-13-1441-2019, 2019.

725   Stanton, T. P., Shaw, W. J., Truffer, M., Corr, H. F. J., Peters, L. E., Riverman, K. L., Bindschadler, R., Holland, D. M., and Anandakrishnan, S.: Channelized Ice Melting in the Ocean Boundary Layer Beneath Pine Island Glacier, Antarctica, Sci., 341, 1236–1239, DOI:10.1126/science.1239373, 2013.

Walker, R. T., Parizek, B. R., Alley, R. B., Anandakrishnan, S., Riverman, K. L., and Christianson, K.: Ice-shelf tidal flexure and subglacial pressure variations, Earth Planet. Sci. Lett., 361, 422–428, https://doi.org/10.1016/j.epsl.2012.11.008, 2013.

730   Washam, P., Nicholls, K. W., Münchow, A., and Padman, L.: Tidal Modulation of Buoyant Flow and Basal Melt Beneath Petermann Gletscher Ice Shelf, Greenland, J. Geophys. Res.-Oceans, 125, https://doi.org/10.1029/2020JC016427, 2020.

Washam, P., Lawrence, J. D., Stevens, C. L., Hulbe, C. L., Horgan, H. J., Robinson, N. J., Stewart, C. L., Spears, A., Quartini, E., Hurwitz, B., Meister, M. R., Mullen, A. D., Dichek, D. J., Bryson, F., and Schmidt, B. E.: Direct observations of melting, freezing, and ocean circulation in an ice shelf basal crevasse, Sci. Adv., 9, DOI:10.1126/sciadv.adi7638, 2023.

735   Whiteford, A., Horgan, H. J., Leong, W. J., and Forbes, M.: Melting and Refreezing in an Ice Shelf Basal Channel at the Grounding Line of the Kamb Ice Stream, West Antarctica, J. Geophys. Res.-Earth Surface, 127, https://doi.org/10.1029/2021JF006532, 2022.

Wilson, E. A., Wells, A. J., Hewitt, I. J., and Cenedese, C.: The dynamics of a subglacial salt wedge, J. Fluid Mech., 895, A20, https://doi.org/10.1017/jfm.2020.308, 2020.

Zhao, K., Skyllingstad, E., and Nash, J. D.: Improved Parameterizations of Vertical Ice-Ocean Boundary Layers and Melt Rates, Geophys.
740   Res. Lett., 51, e2023GL105 862, https://doi.org/10.22541/essoar.169186339.97711746/v1, 2024.